Classification: Biological Sciences / Applied Biological Sciences

Biomimetic engineered muscle with capacity for vascular integration and functional maturation in vivo

Mark Juhas[1], George C. Engelmayr, Jr.[1], Andrew N. Fontanella[1], Gregory M. Palmer[2], and Nenad Bursac[1]*

[1]Department of Biomedical Engineering, Duke University, Durham, NC

[2]Department of Radiation Oncology, Duke University School of Medicine, Durham, NC

*Corresponding author:

Nenad Bursac, PhD
Associate Professor of Biomedical Engineering
Faculty of Cardiology
Duke University
3000 Science Drive
Hudson Hall, Room 136
Durham, NC 27708
phone: 919-660-5510
fax: 919-684-4488
e-mail: nbursac@duke.edu

Keywords: Tissue engineering, skeletal muscle, contractile force, angiogenesis, window chamber

Abstract
Tissue-engineered skeletal muscle can serve as a physiological model of natural muscle and a potential therapeutic vehicle for rapid repair of severe muscle loss and injury. Here we describe a platform for engineering and testing highly functional biomimetic muscle tissues with a resident satellite cell niche and capacity for robust myogenesis and self-regeneration in vitro. Using a mouse dorsal window implantation model and transduction with fluorescent intracellular calcium indicator, gCaMP3, we non-destructively monitored, in real time, vascular integration and the functional state of engineered muscle in vivo. During a 2 week period, implanted engineered muscle exhibited a steady ingrowth of blood-perfused microvasculature along with an increase in amplitude of calcium transients and force of contraction. We also demonstrated superior structural organization, vascularization, and contractile function of fully differentiated vs. undifferentiated engineered muscle implants. The described in vitro and in vivo models of biomimetic engineered muscle represent enabling technology for novel studies of skeletal muscle function and regeneration.

Significance Statement
Engineering of highly functional skeletal muscle tissues can provide accurate models of muscle physiology and disease and aid treatment of various muscle disorders. Previous tissue engineering efforts have failed short of recreating structural and contractile properties of native muscle in vitro. Here we describe the creation of biomimetic skeletal muscle tissues with structural, functional, and myogenic properties characteristic of native muscle and contractile stress values that surpass those of neonatal rat muscle. When implanted and real-time imaged in live animals, engineered muscle grafts undergo robust vascularization and perfusion, exhibit continued myogenesis, and show further improvements in intracellular calcium handling and contractile function. This process is significantly enhanced by myogenic pre-differentiation and formation of aligned muscle architecture in vitro.

Introduction
Natural skeletal muscle consists of terminally differentiated, highly aligned, and contractile myofibers and a population of resident muscle stem cells, known as satellite cells (SCs), which are indispensable for muscle growth (1) and regeneration (2). The ability to create engineered muscle tissues that mimic the structural, functional, and regenerative properties of native muscle would enable design of accurate in vitro models for studies of muscle physiology and development (3, 4) and promote cell-based therapies for muscle injury and disease (5) (6). Pioneering studies of Vandenburgh (7) and Dennis (8) were the first to demonstrate in vitro engineering of functional mammalian muscle constructs, followed by other studies reporting that differentiated engineered muscle can survive and vascularize upon implantation in vivo (9-13). Simultaneously, various studies have shown that compared to differentiated or committed cells, undifferentiated SCs are a more potent myogenic cell source with the ability to engraft and replenish the host satellite cell pool and support future rounds of muscle regeneration (14-16). Thus, it is likely that for optimal therapy, engineered muscle tissues should fully recreate the cellular heterogeneity of native muscle and consist of both force-generating, differentiated myofibers and a functioning SC pool to allow further maturation and regeneration in vivo. Additionally, for long-term survival and efficient repair, implanted engineered muscle constructs must rapidly integrate into host vascular system and significantly increase their functional output compared to pre-implantation levels.

In this study, we utilized primary rat myogenic cells to engineer skeletal muscle tissues with highly organized architecture and force generating capacity comparable to those of native muscle. We characterized the temporal dynamics of myogenic processes within engineered muscle and documented the in vitro formation of a homeostatic tissue state with the co-existence of highly contractile muscle fibers and functional satellite cells. To continuously

monitor engineered tissue survival, function, and vascularization after implantation, we transduced myogenic cells with gCaMP3, a genetic indicator of intracellular Ca^{2+} concentration used previously in neurobiological (17) and cardiac (18) research, and implanted the muscle constructs in a dorsal skinfold chamber in nude mice. The use of this minimally-invasive, in vivo platform allowed us to simultaneously, in real time, quantify and compare changes in Ca^{2+} transient amplitude and vascular density between highly differentiated and undifferentiated engineered muscle implants and to further assess the maintenance of satellite cell pool and enhancement of contractile function relative to those pre-implantation. Overall, our studies describe important advances in the field of skeletal muscle tissue engineering and lay foundation for novel studies of cellular function and signaling in a physiological environment in real time.

Results

Structure of Engineered Muscle. Engineered muscle bundles (Fig. 1*A*) were created using a neonatal rat myogenic cell population that predominantly consisted of $Pax7^+/MyoD^+$ activated satellite cells (SCs) and a small fraction of $myogenin^+$ precursors, but no evidence of endothelial or smooth muscle cells (Fig. S1). After 2 weeks of culture, engineered bundles consisted of laminin-surrounded myofibers that occupied the entire tissue volume (Fig. 1*B*) and a peripheral layer of $vimentin^+$ fibroblasts that resembled the epimysial connective tissue layer encasing the myofibers of neonatal hindlimb muscle (Fig. S2*A*). The interior of both engineered and native neonatal muscle contained densely packed, highly aligned, multinucleated, and cross-striated myofibers surrounded by a basal lamina-like matrix consisting of laminin and collagen IV (Fig. 1*C*). Within the basal lamina, $Pax7^+$ SCs were found residing within a native-like niche, closely abutting myofiber sarcolemma (Fig. 1*C-D,* Fig. S2*B-C*). Overall, the 3D organization of the engineered muscle bundle highly resembled that of a native muscle fascicle, while lacking higher-order structures including multi-fascicle organization, tendons, and neurovascular bed.

Myogenesis in Engineered Muscle. We further quantified the temporal changes in cell proliferation and expression of key myogenic transcription factors (Pax7, MyoD, and myogenin (MyoG)) during in vitro culture (Fig. S3). At early stages of engineered muscle formation (day 2), a large majority of $Pax7^+$ cells (~75%) were activated and proliferating as evidenced by their expression of Ki67 (Fig. S3*A* and *B*). Simultaneously, the vast majority of early fusing cells or newly-formed, multinuclear myotubes expressed MyoD, either without or with MyoG (Fig. S3*C* and *D*). By culture day 14, the cells expressing MyoD alone virtually disappeared and all myonuclei in the engineered muscle expressed MyoG, either alone (~80%) or together with MyoD (Fig. S4*D*). The ~20% $MyoG^+/MyoD^+$ myonuclei located at the periphery or within existing myofibers indicated cells that were either primed for fusion or recently fused. By culture day 14, $Pax7^+$ cells (Fig. S4*A*) remained in relatively high numbers (~20% of all cells) and, as expected, did not co-express MyoG (Fig. S2*C*). Virtually all of the $Pax7^+$ cells were also $MyoD^-$ and quiescent, with only a small fraction (~1.5%) expressing Ki67, suggesting that the engineered muscle attained a differentiated, homeostatic state.

The presence of $MyoD^+$ cells in the homeostatic engineered muscle (Fig. S3*D*) suggested the existence of continuous cell growth and hypertrophy that in native postnatal muscle are supported by creation of new myonuclei via secondary fusion of SCs with myofibers (19). We therefore quantified the temporal changes in myofiber size and SC density at 1, 2, and 4 wks of culture and found significant increase in myofiber diameter (1 wk: 8.73 ± 0.33 μm, 2 wk: 14.9 ± 0.87 μm, 4 wk: 22.2 ± 1.33 μm) accompanied by decreases in SC number per 100 μm of myofiber length (1 wk: 1.22 ± 0.12, 2 wk: 0.75 ± 0.05, 4 wk: 0.52 ± 0.02) (Fig. 1*E*, Fig. S4) indicative of a functioning SC pool and continuous myogenesis. After 4 wk of culture, these

parameters achieved values intermediate between those of neonatal and adult rat muscle tissues (Fig. 1*E*).

Function of Engineered Muscle. In response to electrical stimulation, engineered muscle bundles generated strong twitch contractions that with increase in stimulus frequency fused into a more forceful tetanic contraction (Fig. 1*F*, Fig. S5*A*, Movie S1). As characteristic of native muscle (20), lengthening of engineered muscle yielded a biphasic increase in the amplitude of active (contractile) force and a monotonic increase in passive tension (Fig. 1*G*, Fig. S5*B*). Contractile force generating capacity of engineered muscle increased with time of culture (1 wk: 8.83 ± 2.3 and 17.27 ± 3.6 mN, 2 wk: 17.08 ± 1.1 and 28.39 ± 0.92 mN, 4 wk: 22.79 ± 2.1 and 26.75 ± 2.3 mN (twitch and tetanus), Fig. 1*H*), attaining values more than an order of magnitude higher than those previously reported for other engineered muscle tissues (8, 11, 21-26). Specific tetanic force per unit muscle cross-sectional area of 47.9 ± 4.1 mN/mm^2 in 4-wk engineered bundles surpassed values reported for native neonatal rat soleus muscle (44 mN/mm^2) (20). Moreover, passive tension during 4-wk culture did not change significantly (Fig. S5*C*), yielding high active-to-passive force ratios of ~10-15 (Fig. S5*D*), characteristic of neonatal skeletal muscle (20, 27) and, to our knowledge, unmet in previous tissue engineering studies.

Response of Engineered Muscle to In Vitro Injury. To further investigate the SC function within the engineered muscle, we utilized a cardiotoxin (CTX) injury assay to assess whether the SCs can support muscle self-repair in vitro. Homeostatic, 2-wk old engineered muscle was exposed to 0.2 μM CTX for 6 h and allowed to recover for 10 days. Consistent with in vivo reports (28), the CTX exposure resulted in immediate fragmentation of myofibers, cell death, and disruption of contractile elements leading to a 4-fold decrease in contractile force generation (Fig. 2, Fig. S6). In response to injury, SCs in the engineered muscle underwent robust activation and proliferation such that by 5 days post-injury, initially decreased Pax7$^+$ and MyoD$^+$ cell numbers significantly increased beyond those present in the pre-injury muscle accompanied by a significant rise in the percentage of proliferating SCs (Ki67$^+$/Pax7$^+$) (Fig. 2*B*, Fig. S6*A*-*B*). By 10 days post-injury, numbers of Pax7$^+$, Ki67$^+$/Pax7$^+$, and MyoD$^+$ cells decreased while the number of MyoG$^+$ myonuclei, myofiber density, and % cross-striated myofibers increased to near pre-injury levels (Fig. 2*B*). The progressive regrowth, differentiation, and sarcomerogenesis of engineered muscle fibers resulted in steady recovery of both twitch and tetanic force generation, which by 10 days post-CTX injury reached the near pre-injury levels (Fig 2*B*).

Vascularization of Implanted Engineered Muscle. In order to assess the ability of the engineered muscle to survive and vascularize in vivo, we implanted 2-wk pre-differentiated (PreD) bundles into a dorsal skinfold window chamber in nude mice (29). For this purpose, we generated smaller three-bundle constructs anchored within a single 9x9 mm square Cerex® frame that fit within the window chamber (Fig. 3*A*). As a comparison group, we implanted undifferentiated (UnD) muscle bundles cultured for only 2 d without switching to differentiation media that contained sporadically fusing myotubes and high numbers of Pax7$^+$ and Ki67$^+$ cells (Fig. S7). Placing the engineered muscle between the thin panniculus carnosus muscle layer of the dorsal skin and a cover glass window allowed us to non-destructively, in live animals, track angiogenesis and perfusion of the muscle implant in real time. With time post implantation (PI), initially avascular muscle bundles underwent rapid invasion by host blood vessels (Fig. 3*B*, yellow pseudo-colored region) at a rate that was greater in PreD than in UnD muscle implants, which showed apparent saturation of vessel ingrowth by 14 d PI (Fig. 3*C*). Importantly, all ingrown capillary networks appeared functional and perfused by host blood flow (evident from red blood cell motion) as early as 7 d PI (Movie S2). Interestingly, while asynchronous spontaneous twitches recorded at 2 wk PI had no apparent effect on the blood flow through

ingrown capillaries, occasionally observed spontaneous tetanic contractions appeared to transiently restrict blood perfusion (Movie S3).

Immunostaining analysis (Fig. 3*D*) further revealed randomly oriented vessel networks at the periphery of implanted muscle, while within the implant interior the ingrown capillaries co-aligned with surrounding myofibers to a degree (4.97 ± 1.8°) characteristic of native neonatal muscle (Fig. S8). In addition, in transverse cross-sections, endothelialized vessel lumens were found throughout the full thickness of the implants (Fig. 3*E*). In agreement with intravital imaging analysis, cross-sectional lumen density in both PreD and UnD implant regions increased between 1-wk (PreD: 170 ± 11 per mm^2, UnD: 75 ± 10 per mm^2) and 2-wk (265 ± 30 per mm^2, UnD: 175 ± 18 per mm^2) PI and was significantly higher in PreD implants (Fig. 3*F*). From cross-sectional immunostainings, the average rate of vascular ingrowth in PreD muscle bundles was 18.9 ± 2.1 vessels/mm^2/d. Further, mean lumen diameter increased with time PI, and after 2 wk amounted to 7.1 ± 0.2 µm, similar to values measured in native hindlimb muscle (Fig. S9).

Myogenesis in Implanted Engineered Muscle. After 2 wk in vivo, implanted PreD muscle bundles (identified by GFP^+ staining for gCaMP3) remained separated from the underlying host muscle and appeared to maintain pre-implantation volume and a structure consisting of aligned cross-striated myofibers surrounded by basal lamina proteins (Fig. 3*G-I*). Importantly, the implanted myofibers remained abutted by $Pax7^+$ satellite cells at 2 wk PI, suggesting continued myogenic capacity of engineered muscle in vivo (Fig. 3*J*). Compared to pre-implantation values (i.e., 2-wk in vitro culture (IVC)), PreD bundles at 1 wk PI had less cross-striated myofibers (-40.0 ± 7%); however, by 2 wk PI, virtually all myofibers exhibited cross-striations (Fig. S10) while the PreD myofiber diameter became significantly increased (+40.7 ± 5% relative to IVC). Control UnD muscle bundles that prior to implantation showed only sporadic myofiber formation (Fig. S7 and S10*A*), underwent significant myogenesis over 2 weeks PI; however, their myofiber organization, alignment, diameter, and percent of cross-striated myofibers remained inferior to those of the PreD implants (Fig. S10*B*, Fig. S11,).

Function of Implanted Engineered Muscle. To non-destructively monitor viability and functionality of the engineered muscle in vivo, we lentivirally-transduced intracellular Ca^{2+} sensor gCaMP3 (17) in isolated myogenic cells which allowed us to record spontaneous and electrically-induced Ca^{2+} transients in muscle implant by measuring gCaMP3 fluorescence (ΔF/F, Fig. S12*A-E*). Intravital gCaMP3 fluorescence movies during spontaneous twitching of implanted muscle (Movie S4, Fig. 4*A*) revealed that after an initial lag period of ~7 d, the PreD muscle implants exhibited a steady increase in Ca^{2+} transient amplitude (Fig. 4*B*). The UnD implants, with limited functionality at 2 d PI, also exhibited a steady increase in spontaneous activity and amplitude of Ca^{2+} transients (Fig. 4*B*). Measurements of electrically-induced Ca^{2+} responses in explanted muscle (Movie S5) showed that at 2 wk PI, both PreD and UnD muscle bundles displayed significantly greater Ca^{2+} transient amplitudes compared to their IVC and 1 wk PI counterparts (Fig. 4*C*). Kinetics of gCaMP3 Ca^{2+} transients were not significantly changed between 1 and 2 wk PI and were comparable between the two implant groups (Fig. S13*A*).

Since the implanted engineered muscle underwent robust vascular integration with the host dorsal skin, it could not be separated from the skin without being damaged. Therefore, to eliminate host contribution to the measured contractile force, we implanted engineered muscle bundles in the direction perpendicular to that of the host panniculus carnosus muscle layer (Fig. S13*F-H*). Functional measurements in 1 and 2 wk explants revealed robust contractile force responses in both UnD and PreD groups (Fig. 4*D*). Specifically, implanted engineered UnD muscle steadily increased its force generating capacity in vivo, and after 2 wk PI reached values similar to those measured in the PreD group prior to implantation (Fig. 4*E*). The implanted PreD muscle showed no enhancement in contractile force generation during first wk PI; however, its force generating capacity significantly increased by 2 wk PI, reaching tetanus amplitudes 3.2-

fold higher than the pre-implantation values. This significant increase in the absolute contractile force amplitude was associated with an ~3.8-fold increase in specific force, which at 2 wk PI averaged 65.7 ± 8.9 mN/mm^2. Similar to Ca^{2+} transients, the kinetics of force generation in muscle implants did not significantly change between 1 and 2 wk PI and was comparable between the two implant groups (Fig. S13). Overall, measurements of both Ca^{2+} transient and active force generation suggested that in addition to robust vascularization, implanted engineered muscle underwent significant enhancement of contractile function in vivo, beyond what was achievable in vitro.

Discussion

In this study, we sought to reproduce important aspects of skeletal muscle organogenesis in vitro and create biomimetic tissue constructs with structural, functional, and myogenic properties characteristic of native muscle. Optimizing the cellular and extracellular cues essential for muscle growth and development, we created a 3D culture environment primed for myogenic maturation. Within this engineered muscle environment, initially proliferating Pax7$^+$ and MyoD$^+$ cells underwent rapid fusion and formation of aligned MyoG$^+$ myofibers that attained a highly differentiated phenotype and became surrounded by quiescent Pax7$^+$ SCs residing in native-like niches. Differentiation of SCs during 4-week culture contributed to myofiber hypertrophy, a process characteristic of postnatal muscle growth (19). Along with the structural maturation, contractile capacity of engineered muscle increased beyond specific force values measured in neonatal rat muscle, reaching contractile force amplitude (~30 mN) 10-100 times higher than previously achieved (8, 11, 21-26).

To assess the self-regenerative capacity of engineered muscle, we perturbed its homeostatic state by a short exposure to cardiotoxin, causing significant cell death, myofiber fragmentation, and decline in functional output. Similar to injury response in vivo (30, 31), quiescent SCs in engineered muscle underwent rapid activation and myogenesis to yield efficient structural repair and restoration of contractile function, followed by recovery of myogenic indices to pre-injury values. Collectively, by its ability to support native-like SC function, the 3D engineered muscle tissue described herein may facilitate systematic in vitro studies of SC fate during simulated growth, exercise, injury, or disease (30, 32).

To explore the fate of engineered muscle in vivo, we further combined gCaMP3 transduction with dorsal window chamber studies in live mice and non-invasively monitored the ability of implanted engineered muscle to spontaneously contract, generate Ca^{2+} transients, and undergo blood perfusion over a 2 week period post-implantation. Regarding the rapid development of new fluorescent biosensors of cellular function and signaling (e.g., intracellular ion concentrations, membrane potential, cAMP, pH, etc. (33, 34)), we expect that similar experimental frameworks could allow real-time in vivo studies of various cellular processes of importance for the fields of stem cell and cancer biology, tissue engineering, immunology, and others. In particular, the described concept of simultaneous monitoring of cell viability, intracellular Ca^{2+} concentration, and vascularization within a window chamber environment could be directly applied to *in vivo* studies of Ca^{2+} oscillation-dependent differentiation and function of the heart, neuronal, pancreatic, intestinal, and other cellular and tissue implants.

In our in vivo studies, implanted engineered muscle, showing no evidence of vascular cells at the time of implantation, became progressively infiltrated with host blood vessels and, as evidenced by video-imaging (Movie S2), actively perfused with readily discernible blood cells by 7 days PI. By day 14, the vessel density within the PreD muscle implant (265 ± 30 vessels per mm^2) was comparable to that previously reported for implanted tissue-engineered muscle with pre-formed vascular structures (11) demonstrating that purely angiogenic vessel ingrowth was sufficient to support the in vivo survival and function of small size avascular engineered muscles used in our study. On the other hand, successful survival of large engineered muscles implants will likely require the development of novel methods for in vitro fabrication of highly aligned,

functional, and pre-vascularized skeletal muscle tissues. Related, our preliminary data demonstrate that simple co-encapsulation of myogenic and endothelial cells may significantly impair contractile function of engineered muscle (Fig. S14), suggesting that angiogenic vessel ingrowth rather than simple vasculogenesis may be a desired mode of engineered muscle vascularization, compatible with the formation of biomimetic muscle architecture and function in vitro.

Previously, various cell-based approaches have been explored for treatment of muscle injury or disease (30). Specifically, implanted freshly isolated SCs were found to fuse to existing myofibers, rescue contractile function, and, by homing to the host niche, enhance muscle capacity for endogenous self-repair (14-16). Still, without development of more efficient methods for their expansion in vitro (35, 36), implanted SCs may not be able to undergo timely myogenesis to successfully repair large muscle loss (37) . Implanting readily expandable myoblasts or pre-differentiated myofibers may accelerate in vivo myogenesis, while co-delivery of growth factors may improve cell survival and engraftment (12), however, without SCs, such strategies are likely to provide a limited support for future regenerative events (14, 15, 35). In the current study, we compared the post-implantation fate of PreD muscle constructs consisting of differentiated myofibers and functional SCs with UnD constructs consisting of undifferentiated, proliferative myogenic cells. We found that PreD implants not only exhibited superior structural and functional maturation (evidenced by larger myofiber diameter, percent cross-striations, and contractile force, Fig. 4, Fig. S10, Fig. S11) but also attracted significantly more neovessel ingrowth than UnD implants (Fig. 3*C and F*), possibly due to the increased metabolic demand of more functional myofibers (38). Although these studies utilized a small implant size inadequate for therapeutic muscle replacement, they suggest potential benefits of implanting a functional engineered muscle in which mature myofibers provide niche-like environment for satellite cells compared to sole use of undifferentiated myogenic cells.

Despite a steady increase in vascularization (Fig. 3*C*), the amplitude of spontaneous Ca^{2+} transients in engineered muscle implants started to steadily increase (and correlate with vascular ingrowth (39)) only after an initial lag period of 1 week (Fig. 4*B*). Furthermore, the percentage of cross-striated fibers in PreD implants at 1 week PI was decreased compared to the pre-implantation values (Fig. S10*B*). This adaptation period may have resulted from potential tissue damage caused by initial hypoxia upon implantation into the dorsal window chamber and/or disruption of cell-matrix interactions caused by increased fibrinolysis (in the absence of the antifibrinolyitc supplement amino-caproic acid present in vitro) (26). Nevertheless, by 2 weeks PI, continuous vascularization, myogenesis, and differentiation of the PreD implants led to a ~3-fold increase in force generating capacity compared to pre-implantation values (Fig. 4*E*) yielding specific contractile forces of ~70 mN/mm^2. This in vivo recovery of the engineered muscle function and structural organization followed a similar time-course to that observed in vitro upon CTX-induced injury. Along with the maintenance of aligned, cross-striated myofiber architecture (Fig. 3*I*) and satellite cell pool (Fig. 3*J*), vascularized engineered muscle implants in our study, for the first time to our knowledge, exhibited structure, contractile function, and myogenic capacity representative of post-neonatal skeletal muscle.

In summary, we presented a platform for engineering and studying of highly biomimetic skeletal muscle tissues with functional satellite cells capable of supporting myogenic and self-regenerative events characteristic of native muscle. While initially avascular, these engineered muscle tissues underwent robust vascularization and perfusion, and exhibited continued myogenesis and improved contractile function in vivo, all of which were significantly enhanced by myogenic pre-differentiation of tissue constructs in culture. Together, these results lay a foundation for novel in vitro and in vivo studies of skeletal muscle function, regeneration, and vasculogenesis and provide a blueprint for future engineering of 3D functional human muscle microtissues for drug and toxicology studies (4) (40).

Materials and Methods

All methods are described in detail within Supporting Information Appendix.

Engineering of Muscle Bundles. Large single muscle bundles and smaller tri-bundle muscle implants were formed within polydimethylsiloxane (PDMS) molds as previously described (26, 41). Cell/hydrogel mixture (Table S1) was injected into the PDMS molds, polymerized at 37°C for 45 min, and cultured on a rocker at 37°C for up to 4 wks.

In Vitro Cardiotoxin Injury Assay. Following 2 weeks of in vitro culture, differentiated engineered muscle bundles were exposed to 0.2 μM cardiotoxin (CTX, Cardiotoxin from *Naja mossambica mossambica*, Sigma) for 6 hours on a rocker at 37°C. The injured bundles were then rinsed 3 times to remove the toxin and re-incubated in fresh differentiation medium. Cardiotoxin-injured bundles were assessed for structural composition and contractile function immediately after CTX removal ('6h post-CTX' group) and following culture in differentiation media for additional 5 or 10 days ('5d post-CTX' and '10d post-CTX' groups).

Implantation of Engineered Muscle. All animal experiments were approved by the Duke University ACUC. A circular region (~12 mm) of the forward-facing dorsal skin of nude mice was dissected away and a tri-bundle muscle construct was laid perpendicular to the muscle on the rearward-facing skin (Fig. S14), providing a source of host microvessels (29).

Intravital Imaging of Blood Vessels and Intracellular Ca^{2+} Transients. Intravital recordings were performed at 5X magnification on days 2, 5, 7, 9, 12, and 14 post-implantation (PI). Capillary vessels were imaged by a video camera and analyzed from total hemoglobin images (29). Spontaneous Ca^{2+} transients reported by gCaMP3 (17) fluorescence were imaged by a fast CCD camera and analyzed as previously described (25).

In Vitro and Ex Vivo Force Measurements. Engineered muscle constructs were loaded into a custom-made force measurement setup containing an optical force transducer and a linear actuator (ThorLabs), as previously described (25, 26, 42). Samples were stimulated (10 ms, 3V/mm pulses) at different frequencies (1-40 Hz), and isometric passive and active (contractile) forces were measured at different muscle lengths. Kinetics of contraction and specific force were calculated as previously described (26).

Acknowledgements
We acknowledge R. Kirkton, W. Bian, S. Hinds, E. Krol, A. Ganapathi, and L. Li for their technical support. This study was supported by the National Science Foundation's Graduate Research Fellowship to M. Juhas and grant AR055226 from National Institute of Arthritis and Musculoskeletal and Skin Diseases to N. Bursac.

References

1. Kuang S, Charge SB, Seale P, Huh M, & Rudnicki MA (2006) Distinct roles for Pax7 and Pax3 in adult regenerative myogenesis. *J Cell Biol* 172(1):103-113.
2. Lepper C, Partridge TA, & Fan CM (2011) An absolute requirement for Pax7-positive satellite cells in acute injury-induced skeletal muscle regeneration. *Development* 138(17):3639-3646.

3. Cosgrove BD, Sacco A, Gilbert PM, & Blau HM (2009) A home away from home: challenges and opportunities in engineering in vitro muscle satellite cell niches. *Differentiation; research in biological diversity* 78(2-3):185-194.
4. Vandenburgh H (2010) High-content drug screening with engineered musculoskeletal tissues. *Tissue engineering. Part B, Reviews* 16(1):55-64.
5. Juhas M & Bursac N (2013) Engineering skeletal muscle repair. *Current opinion in biotechnology* 24(5):880-886.
6. Rossi CA, Pozzobon M, & De Coppi P (2010) Advances in musculoskeletal tissue engineering: moving towards therapy. *Organogenesis* 6(3):167-172.
7. Shansky J, Del Tatto M, Chromiak J, & Vandenburgh H (1997) A simplified method for tissue engineering skeletal muscle organoids in vitro. *In vitro cellular & developmental biology. Animal* 33(9):659-661.
8. Dennis RG & Kosnik PE, 2nd (2000) Excitability and isometric contractile properties of mammalian skeletal muscle constructs engineered in vitro. *In vitro cellular & developmental biology. Animal* 36(5):327-335.
9. Levenberg S*, et al.* (2005) Engineering vascularized skeletal muscle tissue. *Nature biotechnology* 23(7):879-884.
10. Thorrez L*, et al.* (2006) Angiogenesis enhances factor IX delivery and persistence from retrievable human bioengineered muscle implants. *Molecular therapy : the journal of the American Society of Gene Therapy* 14(3):442-451.
11. Koffler J*, et al.* (2011) Improved vascular organization enhances functional integration of engineered skeletal muscle grafts. *Proceedings of the National Academy of Sciences of the United States of America* 108(36):14789-14794.
12. Borselli C, Cezar CA, Shvartsman D, Vandenburgh HH, & Mooney DJ (2011) The role of multifunctional delivery scaffold in the ability of cultured myoblasts to promote muscle regeneration. *Biomaterials* 32(34):8905-8914.
13. Corona BT, Ward CL, Baker HB, Walters TJ, & Christ GJ (2013) Implantation of In Vitro Tissue Engineered Muscle Repair Constructs and Bladder Acellular Matrices Partially Restore In Vivo Skeletal Muscle Function in a Rat Model of Volumetric Muscle Loss Injury. *Tissue engineering. Part A*.
14. Montarras D*, et al.* (2005) Direct isolation of satellite cells for skeletal muscle regeneration. *Science* 309(5743):2064-2067.
15. Rossi CA*, et al.* (2011) In vivo tissue engineering of functional skeletal muscle by freshly isolated satellite cells embedded in a photopolymerizable hydrogel. *FASEB journal : official publication of the Federation of American Societies for Experimental Biology* 25(7):2296-2304.
16. Sacco A, Doyonnas R, Kraft P, Vitorovic S, & Blau HM (2008) Self-renewal and expansion of single transplanted muscle stem cells. *Nature* 456(7221):502-506.
17. Tian L*, et al.* (2009) Imaging neural activity in worms, flies and mice with improved GCaMP calcium indicators. *Nature methods* 6(12):875-881.
18. Shiba Y*, et al.* (2012) Human ES-cell-derived cardiomyocytes electrically couple and suppress arrhythmias in injured hearts. *Nature* 489(7415):322-325.
19. Davis TA & Fiorotto ML (2009) Regulation of muscle growth in neonates. *Curr Opin Clin Nutr* 12(1):78-85.
20. Close R (1964) Dynamic Properties of Fast + Slow Skeletal Muscles of Rat during Development. *J Physiol-London* 173(1):74-&.
21. Yan W*, et al.* (2007) Tissue engineering of skeletal muscle. *Tissue engineering* 13(11):2781-2790.
22. Williams ML, Kostrominova TY, Arruda EM, & Larkin LM (2013) Effect of implantation on engineered skeletal muscle constructs. *Journal of tissue engineering and regenerative medicine* 7(6):434-442.

23. Huang YC, Dennis RG, Larkin L, & Baar K (2005) Rapid formation of functional muscle in vitro using fibrin gels. *J Appl Physiol* 98(2):706-713. Epub 2004 Oct 2008.
24. Carosio S*, et al.* (2013) Generation of eX vivo-vascularized Muscle Engineered Tissue (X-MET). *Scientific reports* 3:1420.
25. Bian W & Bursac N (2012) Soluble miniagrin enhances contractile function of engineered skeletal muscle. *FASEB journal : official publication of the Federation of American Societies for Experimental Biology* 26(2):955-965.
26. Hinds S, Bian W, Dennis RG, & Bursac N (2011) The role of extracellular matrix composition in structure and function of bioengineered skeletal muscle. *Biomaterials* 32(14):3575-3583.
27. Mutungi G, Trinick J, & Ranatunga KW (2003) Resting tension characteristics in differentiating intact rat fast- and slow-twitch muscle fibers. *Journal of Applied Physiology* 95(6):2241-2247.
28. Couteaux R, Mira JC, & d'Albis A (1988) Regeneration of muscles after cardiotoxin injury. I. Cytological aspects. *Biology of the cell / under the auspices of the European Cell Biology Organization* 62(2):171-182.
29. Palmer GM*, et al.* (2011) In vivo optical molecular imaging and analysis in mice using dorsal window chamber models applied to hypoxia, vasculature and fluorescent reporters. *Nature protocols* 6(9):1355-1366.
30. Yin H, Price F, & Rudnicki MA (2013) Satellite cells and the muscle stem cell niche. *Physiological reviews* 93(1):23-67.
31. Dhawan J & Rando TA (2005) Stem cells in postnatal myogenesis: molecular mechanisms of satellite cell quiescence, activation and replenishment. *Trends in cell biology* 15(12):666-673.
32. Sacco A*, et al.* (2010) Short telomeres and stem cell exhaustion model Duchenne muscular dystrophy in mdx/mTR mice. *Cell* 143(7):1059-1071.
33. Tantama M, Hung YP, & Yellen G (2012) Optogenetic reporters: Fluorescent protein-based genetically encoded indicators of signaling and metabolism in the brain. *Progress in brain research* 196:235-263.
34. Okumoto S, Jones A, & Frommer WB (2012) Quantitative imaging with fluorescent biosensors. *Annual review of plant biology* 63:663-706.
35. Gilbert PM*, et al.* (2010) Substrate elasticity regulates skeletal muscle stem cell self-renewal in culture. *Science* 329(5995):1078-1081.
36. Urbani L, Piccoli M, Franzin C, Pozzobon M, & De Coppi P (2012) Hypoxia increases mouse satellite cell clone proliferation maintaining both in vitro and in vivo heterogeneity and myogenic potential. *PloS one* 7(11):e49860.
37. Turner NJ & Badylak SF (2012) Regeneration of skeletal muscle. *Cell and tissue research* 347(3):759-774.
38. Fraisl P, Mazzone M, Schmidt T, & Carmeliet P (2009) Regulation of angiogenesis by oxygen and metabolism. *Developmental cell* 16(2):167-179.
39. Lee SL, Pevec WC, & Carlsen RC (2001) Functional outcome of new blood vessel growth into ischemic skeletal muscle. *Journal of vascular surgery* 34(6):1096-1102.
40. Truskey G*, et al.* (2013) Design considerations for an integrated microphysiological muscle tissue for drug and tissue toxicity testing. *Stem Cell Research & Therapy* 4(Suppl 1)(S10):1-5.
41. Bian W, Liau B, Badie N, & Bursac N (2009) Mesoscopic hydrogel molding to control the 3D geometry of bioartificial muscle tissues. *Nature protocols* 4(10):1522-1534.
42. Liau B, Christoforou N, Leong KW, & Bursac N (2011) Pluripotent stem cell-derived cardiac tissue patch with advanced structure and function. *Biomaterials* 32(35):9180-9187.

Figure Legends

Fig.1. Structural and functional characterization of in vitro engineered skeletal muscle. (*A*) Live image of a 2-wk engineered muscle bundle (~1.5 mm diameter, 1.25 cm long) anchored at ends by tendon-mimetic Velcro tabs pinned inside polydimethylsiloxane (PDMS) well. (*B*) Immunostained bundle cross-section shows F-actin$^+$ myofibers embedded within laminin (Lam) rich matrix. (*C*) Structural organization of representative engineered and native neonatal rat soleus muscles (inset: transverse Col4$^+$ structures present in native but not engineered muscle are CD31$^+$ blood vessels). SAA, sarcomeric α-actin; Col4, collagen IV. (*D*) Pax7$^+$ satellite cells in engineered muscle reside at myofiber sarcolemma. (*E*) Average myofiber diameter and SC number per 100 μm myofiber length at 1, 2, and 4 wk of culture compared to native neonatal (neo) and adult soleus muscles. (*F*) Dependence of active force amplitude (normalized to that of single twitch) on stimulus frequency. (*G*) Dependence of active twitch and passive tension amplitudes on engineered muscle length (expressed relative to culture length). (*H*) Absolute and specific (force per area) twitch (Tw) and tetanus (Tet, 40 Hz) amplitudes in engineered bundles at 1, 2, and 4 wk of culture. Mean ± SEM; *n* = 4-10 samples per group (8-10 images per sample); **P < 0.01 between 4 wk bundle and native muscles; P < 0.05 between denoted groups.

Fig. 2. Regenerative response of engineered muscle to in vitro cardiotoxin (CTX) injury. (*A*) Representative images of engineered muscle structure, and Pax7$^+$ cells with time post-CTX injury (induced at 14 d of culture). (*B*) Pax7$^+$, Ki67$^+$/Pax7$^+$ (% of Pax7$^+$), MyoD$^+$, and myogenin (MyoG)$^+$ cell density, myofiber density, % cross-striated myofibers and twitch and tetanus force amplitudes shown relative to pre-injury levels at 6 h, 5 d, and 10 d post CTX addition. Mean ± SEM; *n* = 3-5 samples per group (6-10 images per sample); *P < 0.05 compared to 2 week healthy controls; P < 0.05 between denoted groups.

Fig. 3. Vascular integration of implanted engineered muscle. (*A*) Implanted muscle patch within the dorsal skin-fold window chamber. (*B*) Images of total hemoglobin at d 2, 9, and 14 in window chamber (yellow = implant region). (*C*) Fold change in blood vessel density (BVD) in the implant region of pre-differentiated (PreD) and undifferentiated (UnD) bundles with time PI. (*D*) Vessel organization at the periphery and interior of muscle implant. CD31 labels endothelial cells. (*E*) Cross-section of the muscle implant showing lumens of ingrown blood vessels (arrowheads); VWF, Von Wilenbrand factor. (*F*) Increase of cross-sectional BVD from 1 wk PI to 2 wk PI. Mean ± SEM; *n* = 8-12 per group; *P < 0.05 from value at d 2, $^{\#}$P < 0.05 between PreD and UnD groups at same time-point, P < 0.05 between denoted groups. (*G*) Cross-section of implant region (GFP-positive myofibers) and underlying host muscle. (*H-I*) Longitudinal section of implanted bundle showing aligned and cross-striated myofibers (*H*) embedded in laminin matrix (*I*). (*J*) Pax7$^+$ satellite cells (arrowheads) are found at the periphery of implanted myofibers.

Fig. 4. Calcium transients and force generation of implanted engineered muscle. (*A*) Representative intravital snapshots of a gCaMP3 movie recorded during spontaneous activity of an implanted muscle bundle. Traces below panels show time course of gCaMP3 signal from a small bundle region (square) with lines denoting the snapshot times. Average amplitudes of *in vivo* spontaneous (*B*) and *ex-vivo* electrically-induced (*C*) gCaMP3 transients in implanted PreD and UnD engineered muscle with time PI. IVC, 2 wk of *in vitro* culture, prior to implantation. Representative tetanus force traces (*D*) and quantified (*E*) twitch and tetanus force amplitudes for PreD and UnD muscle cultured *in vitro* (IVC) or explanted at 1 wk PI and 2 wk PI. Mean ± SEM; *n* = 6-12 bundles per group; $^{\#}$P < 0.05 and $^{\#\#}$P < 0.001 between PreD and UnD group at

same time-point; *P < 0.05 and **P < 0.001 compared to PreD IVC group; P < 0.05 and P < 0.001 between groups identified by horizontal solid and dashed lines, respectively.

Figure 1

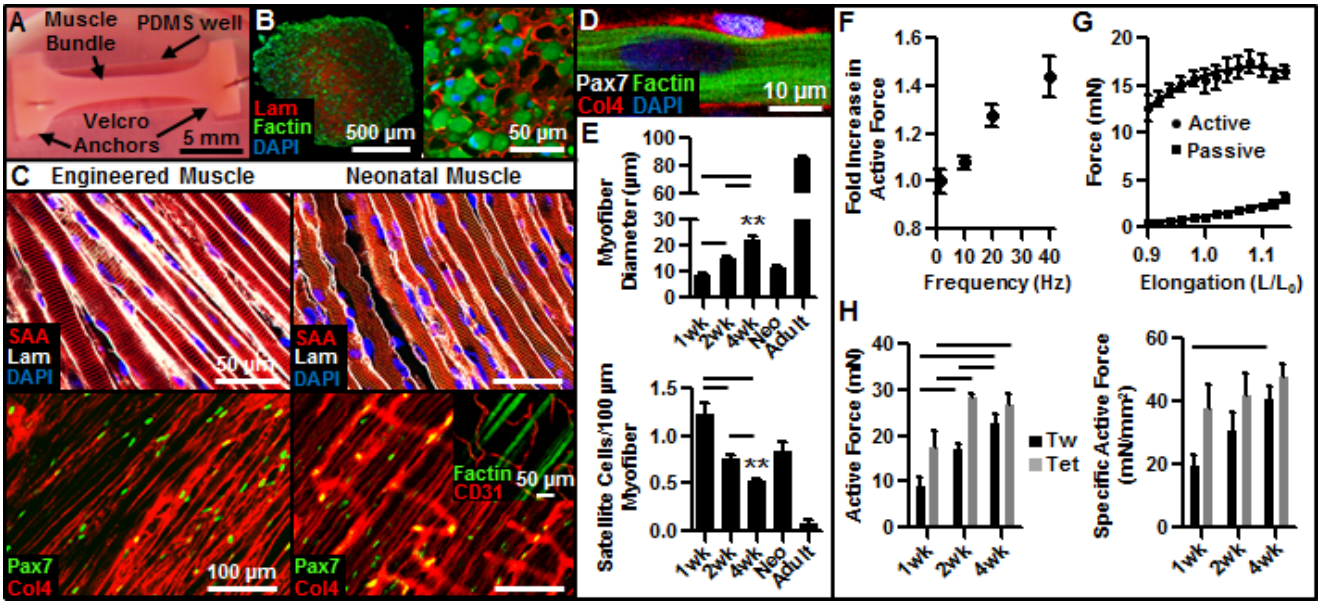

Figure 2

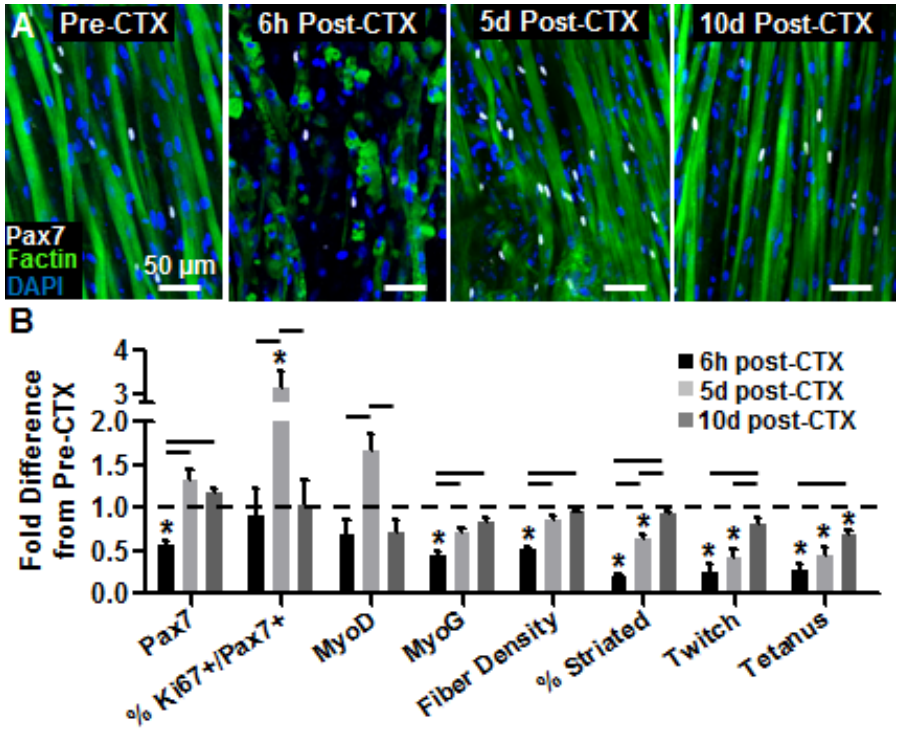

Figure 3

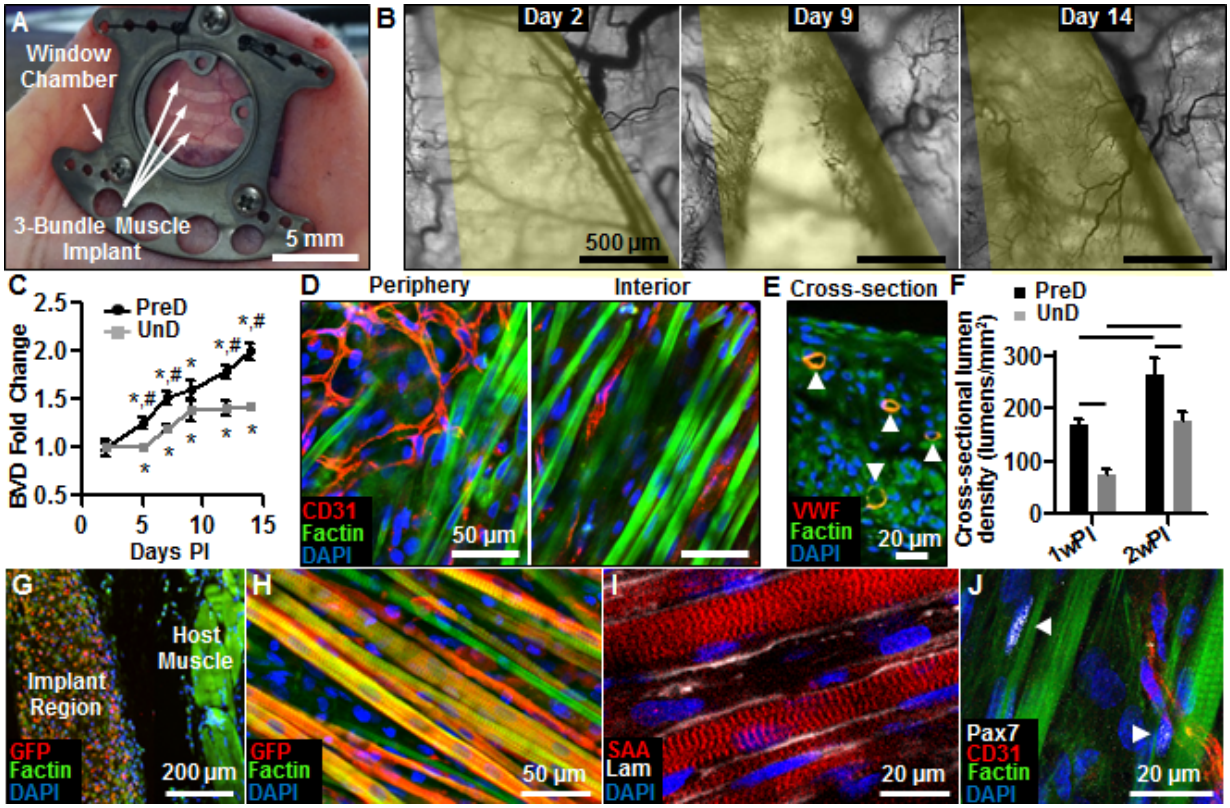

Figure 4

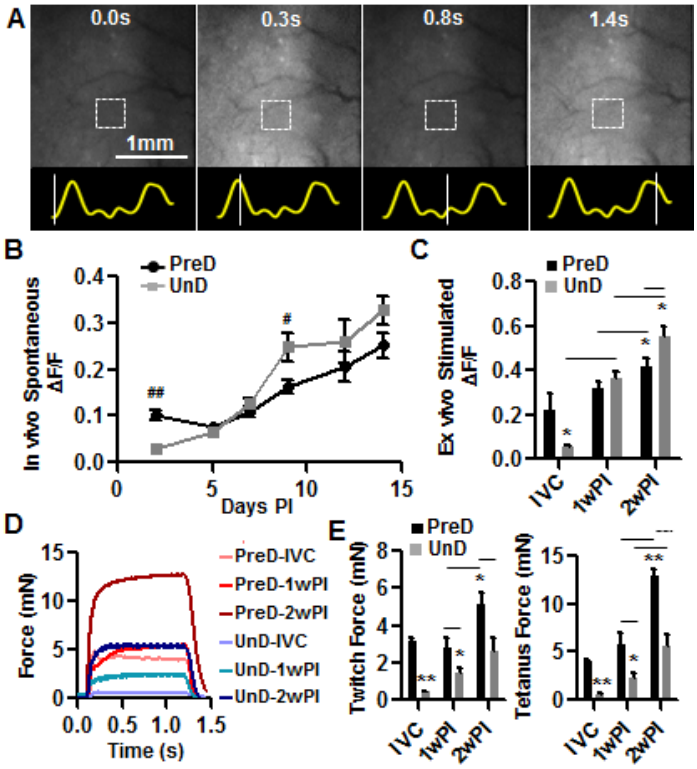

Supporting Information Appendix

Juhas *et al.*

Appendix Contents:

1) SI Materials and Methods

Cell Isolation and GCaMP3 Transduction. Muscle tissue from the lower hind limbs of 2-3-d-old Sprague-Dawley rats was digested with 1 mg/mL collagenase (Worthington) and 2% dispase ((v/v), BD) in Wyles solution (Table S1) for 1 h at 37°C on a rocker, as previously described (1). Isolated cells were resuspended in growth medium (Table S1), and preplated for 2 h at 37°C to reduce fraction of faster-adhering fibroblasts. The supernatant was then seeded on Matrigel coated flasks, and following day cells were reconstituted in growth media, transduced with a GCaMP3 lentivirus, and after 24 h, detached by 2% dispase (v/v) and used for generation of engineered muscle bundles. The implanted GCaMP3$^+$ muscle bundles were identified following staining with anti-GFP (Abcam) antibody.

Engineering of Muscle Bundles. Large single muscle bundles and smaller tri-bundle muscle implants were formed within polydimethylsiloxane (PDMS) molds containing a single semi-cylindrical well (1.25 cm long, 3 mm diameter) or three semi-cylindrical wells (7 mm long, 2 mm diameter), respectively, cast from 3D-machined Teflon masters. PDMS molds were coated with 0.2% (w/v) pluronic (Invitrogen) to prevent hydrogel adhesion. For single bundles, two Velcro felts (2mm x 4mm) were pinned at ends of the wells to anchor the hydrogel. Similarly, for tri-bundle implants, laser-cut Cerex® frames (9 mm x 9 mm, 1 mm wide rim) positioned around the 3 wells enabled hydrogel attachment and facilitated construct handling and implantation. Cell/hydrogel mixture (Table S1) was injected into the PDMS wells, polymerized at 37°C for 45 min, and cultured on a rocker at 37°C for 2-4 wk. After 4 d of culture, growth medium was replaced by differentiation medium (Table S1) to promote fusion and differentiation of the myogenic cells into myofibers. Degradation of fibrin was inhibited by 1 mg/mL aminocaproic acid (Sigma). Cell-mediated hydrogel compaction generated passive tension resulting in uniaxial cell alignment (2, 3).

Implantation of Engineered Muscle Bundles. All animal experiments were approved by the Duke University ACUC. Nude mice (~10 wk of age; 22-30 g) were anesthetized by intraperitoneal injection of ketamine (100 mg/kg) and xylazine (10 mg/kg). Using aseptic technique, the dorsal skin was attached to a temporary "C-frame" at the center of the back. The skin was perforated in three locations to accommodate the screws of the chamber, and a circular region (~12 mm) of the forward-facing skin (i.e., cutis, subcutis, retractor and panniculus carnosis muscles, and associated fascia) was dissected away to accommodate the window proper. The forward and rearward pieces of the titanium dorsal skinfold chamber were assembled together from opposite sides of the skin, and a Cerex® frame with tri-bundle muscle constructs was laid perpendicular (verified under microscope) to the intact panniculus carnosis muscle of the rearward-facing skin (Fig. S12*F-G*), providing a source of microvessels for vascularization. A sterile cover glass was placed over the window and engineered tissue while superfusing with sterile saline solution. The chamber was then secured with suture and the “C-frame” was removed. Post-operatively, the mouse was injected subcutaneously with buprenorphine (1 mg/kg) painkiller and let to recover on a heating pad (4).

Intravital Imaging of Blood Vessels. Intravital recordings were performed in anesthetized mice on d 2, 5, 7, 9, 12, and 14 post-implantation (PI). Mice were anesthetized by nose cone

inhalation of isoflurane and positioned on a heating pad under a microscope objective. Hyperspectral brightfield image sequences (10 nm increments from 500 – 600 nm) were captured at 5x magnification using a tunable filter (Cambridge Research & Instrumentation, Inc.) and a DVC camera (ThorLabs), as previously described (4). A custom MATLAB (MathWorks) script was applied to create maps of total hemoglobin concentration (Fig. S15). Obtained maps were further processed using local contrast enhancement in ImageJ (FIJI) and thresholded to binary images to identify vessel area and calculate blood vessel density (BVD, total area of blood vessels per bundle area).

Intravital Imaging of Intracellular Ca^{2+} Transients. Intravital imaging of spontaneous Ca^{2+} transients was performed immediately after vessel imaging with mice still anesthetized. Fluorescent GCaMP3 signals in implanted bundles were video-imaged through a FITC-filter using a fast fluorescent camera (Andor; at 16 μm spatial and 20 ms temporal resolution). Amplitudes of spontaneous Ca^{2+} transients were determined using the Solis software (Andor) by averaging relative fluorescence intensity (ΔF/F) from three ~400x400 μm^2 regions within each bundle (Fig. S12*C*) (5).

In Vitro and Ex Vivo Measurements of Ca^{2+} Transients. Electrically-induced GCaMP3 Ca^{2+} transients were imaged in engineered muscle bundles after 2 and 14 d of in vitro culture and in muscle explants 1 and 2 wk PI. Engineered muscle constructs were transferred into a custom chamber mounted on an inverted fluorescence microscope (Nikon), placed in 37°C Tyrode's solution (Table S1), and electrically stimulated (10 ms pulse, 3 V/mm). Induced GCaMP3 signals were recorded using a fast fluorescent camera Andor iXon 860 EMCCD (24 μm spatial and 20 ms temporal resolution) and analyzed as described for intravital assessment. Kinetics of Ca^{2+} transients were also characterized as previously described (5).

Immunostaining. Cultured cells were fixed in 4% paraformaldehyde (PFA, 15 min, RT). Whole muscle constructs and native muscle tissues were fixed overnight (4°C) in 2% PFA. Fixed samples were washed in PBS, and placed in blocking solution (Table S1) overnight (4°C). Samples were incubated in primary antibodies (Table S2) for 24 h (4°C), washed in PBS, and incubated in secondary antibodies (Table S2) for 2 h (37°C). Images were acquired using a Zeiss confocal microscope. Tissues used for cross-sectional staining were embedded in paraffin, sectioned (5 μm), washed with xylene, rehydrated, microwaved 5 times for 3 m in a citrate buffer solution (Table S1), and immunostained.

Analysis of Nuclear Counts. To automate nuclear counting, we utilized a custom MATLAB image processing program (6) that allows user-thresholding of DAPI or transcription factor (Pax7, Ki67, MyoD, myogenin) staining and, based on the median size of nuclei for a given magnification, designates and counts identified nuclei. The program outputs the processed images with identified nuclei for the manual verification by user.

Analysis of Myofiber and Blood Vessel Alignment. Orientation of muscle fibers (marked by expression of GFP or F-actin) and blood vessels (marked by expression of CD31) was quantified in engineered muscle implants and native muscle from confocal images acquired at 20x magnification using a previously described image intensity gradient algorithm (3, 6). Local feature orientation was calculated within 25x25 pixel (11x11 μm) subregions (Fig. S8) in which

myofibers or blood vessels were present and standard vessel angle deviation and absolute mean fiber angle difference between myofiber and vessel directions were calculated by averaging subregion data over the entire (450x450 μm) image. Four images were analyzed per each muscle sample.

Statistics. Results are presented as mean ± SEM. Statistical significances among different groups were evaluated by unpaired t-test or one-way ANOVA with post hoc Tukey's test using GraphPad Prism (GraphPad Software, Inc.). $P<0.05$ was consider statistically significant. Different levels of significance were noted in figures and figure captions.

References

1. Bian W & Bursac N (2009) Engineered skeletal muscle tissue networks with controllable architecture. *Biomaterials* 30(7):1401-1412.
2. Hinds S, Bian W, Dennis RG, & Bursac N (2011) The role of extracellular matrix composition in structure and function of bioengineered skeletal muscle. *Biomaterials* 32(14):3575-3583.
3. Bian W, Liau B, Badie N, & Bursac N (2009) Mesoscopic hydrogel molding to control the 3D geometry of bioartificial muscle tissues. *Nature protocols* 4(10):1522-1534.
4. Palmer GM*, et al.* (2011) In vivo optical molecular imaging and analysis in mice using dorsal window chamber models applied to hypoxia, vasculature and fluorescent reporters. *Nature protocols* 6(9):1355-1366.
5. Bian W & Bursac N (2012) Soluble miniagrin enhances contractile function of engineered skeletal muscle. *FASEB journal : official publication of the Federation of American Societies for Experimental Biology* 26(2):955-965.
6. Badie N, Satterwhite L, & Bursac N (2009) A method to replicate the microstructure of heart tissue in vitro using DTMRI-based cell micropatterning. *Annals of biomedical engineering* 37(12):2510-2521.

2) SI Tables.

Table S1. Cell Culture Media and Solutions

Name	Details
Blocking solution	5% chicken serum, 0.2% Triton-X (Sigma)
Cell/hydrogel mixture	10 million cells/mL, 2x growth medium, 4 mg/mL bovine fibrinogen (Sigma), Matrigel (20% v/v)), thrombin (0.2 unit/mg fibrinogen, Sigma)
Citrate Buffer Solution	90% H_2O, 8% 100mM Sodium Citrate, 2% 100mM Citric Acid
Differentiation Medium	DMEM, 3% (v/v) horse serum, 50 unti/mL penicillin G, 50 ug/mL strepomycin, 5 ug/mL gentamicin
Growth Medium	Dulbecco's modified Eagle's medium (DMEM), 10% (v/v) fetal bovine serum, 50 unti/mL penicillin G, 50 ug/mL strepomycin, 5 ug/mL gentamicin
Tyrode's Solution	135 mM NaCl, 5.4 mM KCl, 1.8 mM CaCl, 1 mM MgCl, 0.33 mM NaHPO, 5 mM HEPES, 5 mM glucose
Wyles Solution	137 mM NaCl, 5 mM KCl, 21 mM HEPES, 0.7 mM Na2HPO4, 100 mM glucose, 0.1 mg/mL BSA

Table S2. Antibody List

Primary Epitope	Dilution	Supplier	Catalog no.
Pax7	1:15	Developmental Studies Hybridoma Bank	Pax7-s
MyoD	1:200	BD Pharmingen	554130
myogenin	1:200	Santa Cruz Biotechnology	sc-576
sarcomeric α-actinin	1:200	Sigma	a7811
collagen IV	1:300	Abcam	ab6586
laminin	1:300	Abcam	ab11575
vimentin	1:400	Sigma	v6630
CD31	1:300	Abcam	ab28364
VWF	1:200	Abcam	ab6994
Ki67	1:200	Abcam	Ab15580
Secondary Epitope	**Dilution**	**Supplier**	**Catalog no.**
Alexa Fluor 488 Phalloidin	1:300	Life Technologies	A12379
Alexa Fluor 594 Chicken Anti-Mouse IgG	1:200	Life Technologies	A21201
Alexa Fluor 594 Chicken Anti-Rabbit IgG	1:201	Life Technologies	A21442
Alexa Fluor 647 Chicken Anti-Mouse IgG	1:202	Life Technologies	A21463
Alexa Fluor 488 Chicken Anti-Mouse IgG	1:203	Life Technologies	A21200

3) SI Figures

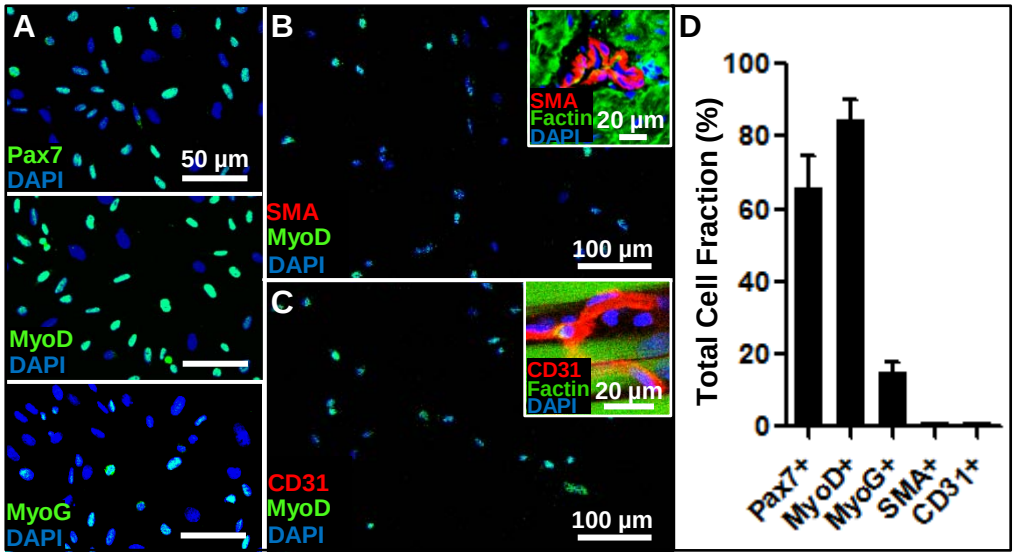

Fig. S1. Input cell population for engineering of skeletal muscle bundles. (*A*) Representative immunostaining of Pax7$^+$, MyoD$^+$, and myogenin (MyoG)$^+$ cells. (*B-C*) No α-smooth muscle actin (SMA)$^+$ smooth muscle cells (*A*) or CD31$^+$ endothelial cells (*B*) were present in the cell isolates. Insets, positive controls for SMA and CD31 antibodies showing a blood vessel in adult rat cardiac muscle (*A*) and capillaries in native neonatal rat skeletal muscle (*B*). (*D*) Quantified fractions of myogenic (Pax7$^+$, MyoD$^+$, MyoG$^+$) and vasculogenic (SMA$^+$, CD31$^+$) cells used for engineering of skeletal muscle (n = 3 cell isolations). Stainings suggest that cell population consists primarily of activated satellite cells (SCs), a proliferative population of Pax7$^+$/MyoD$^+$ cells that can either commit to a myoblast fate (Pax7$^-$/MyoD$^+$) or revert to the quiescent state (Pax7$^+$/MyoD$^-$) characteristic of homeostatic native muscle.

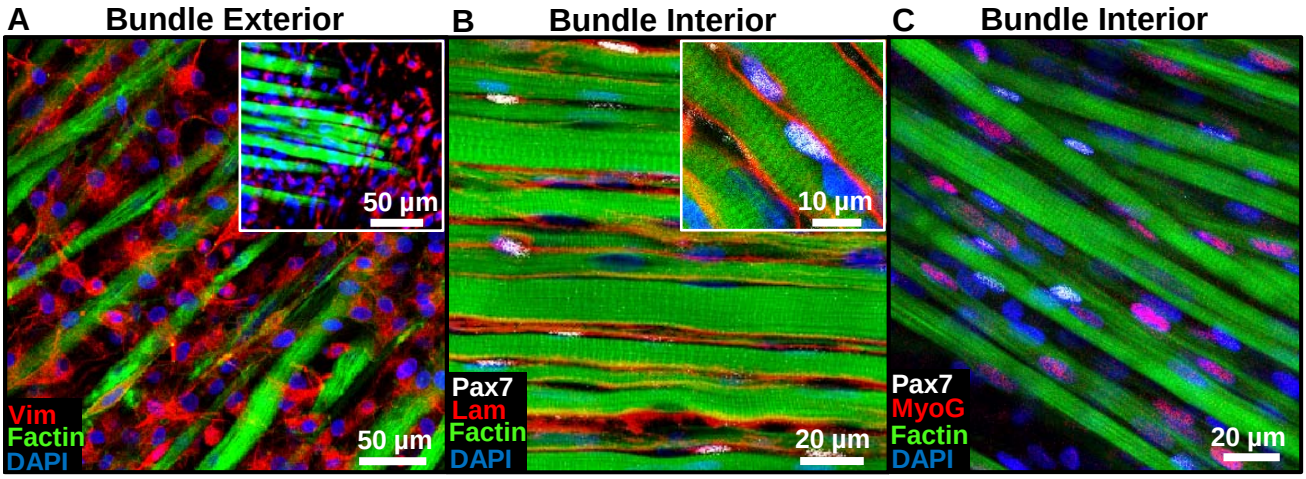

Fig. S2. Structural organization of engineered muscle bundles. (*A*) Representative image of the exterior of a 2-wk old engineered muscle bundle showing an outer layer of vimentin$^+$ fibroblasts; inset: staining of the epimysial region of the neonatal rat soleus muscle showing similar fibroblast abundance. (*B*) Representative image of the interior of a 2-wk old engineered muscle bundle consisting of aligned striated myofibers and abutting Pax7$^+$ satellite cells (SCs) residing within a laminin-rich (Lam) matrix; inset: close-up of neonatal rat soleus muscle showing similar position of SCs beneath basal lamina. (*C*) Representative image of the distribution of SCs and myonuclei (MyoG$^+$ nuclei) in a 2-wk old engineered muscle bundle.

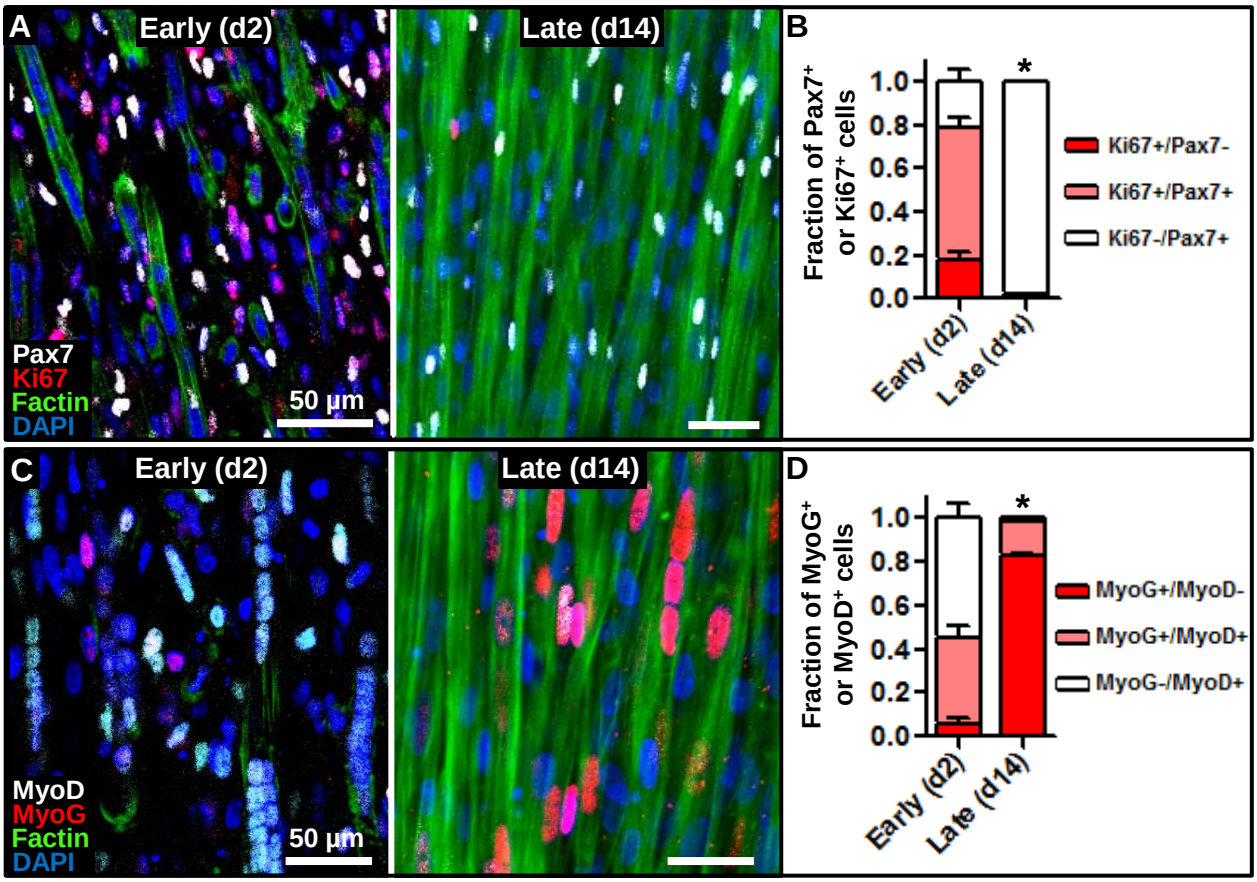

Fig. S3. Acquisition of homeostatic cell composition within engineered muscle bundles. (*A*) Representative images of Pax7 and Ki67 expression inside the engineered muscle bundles at early fusion (2d) and late post-differentiation (14d) times during in vitro culture. (*B*) Quantified fractions of $Pax7^+$ and/or $Ki67^+$ cells at 2 and 14 days of culture. Note a homeostatic shift to a non-proliferative quiescent muscle phenotype at 14d of culture. (*C*) Representative MyoD and myogenin (MyoG) expression inside the engineered muscle bundles at 2 and 14 days of culture. Note that abundant expression of MyoD in early fusing myofibers at culture day 2 is significantly decreased with the formation of mature myofibers by day 14. (*D*) Quantified fractions of $MyoD^+$ and/or $MyoG^+$ cells demonstrate switch to a mature, differentiated muscle phenotype. Mean ± SEM; *n* = 3-6 bundles per group; P*<0.05 compared to corresponding early time-point for each group.

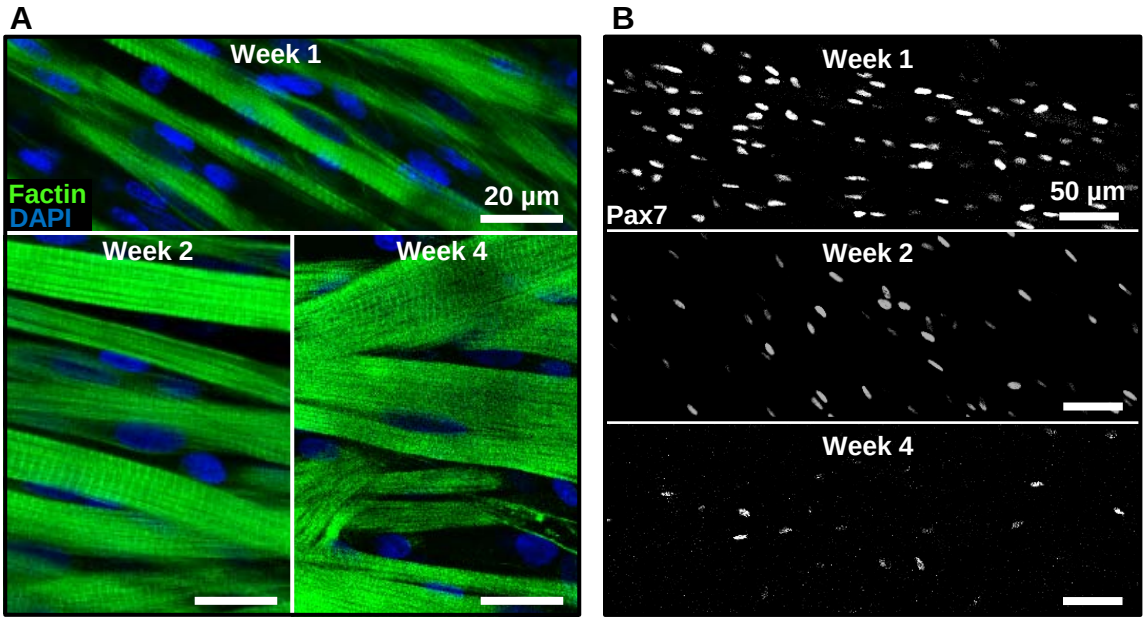

Fig. S4. Myofiber hypertrophy in engineered muscle bundles. (*A*,*B*) Representative images of the steady increase in myofiber diameter (*A*) and decrease in Pax7^{+} SC number (*B*) within engineered muscle bundles over 4 wk culture.

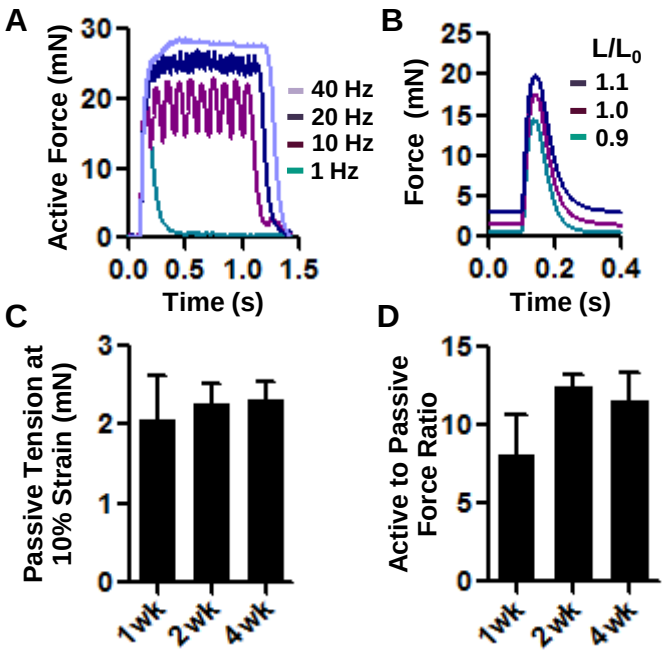

Fig. S5. Functional characterization of engineered muscle bundles. (*A*) Representative active force traces in 2-wk old engineered muscle bundles showing increase in active force amplitude and generation of tetanic contraction at increased frequency of electrical stimulation. (*B*) Representative twitch force traces in 2-wk old engineered muscle bundles showing changes in active twitch and passive tension amplitudes with increase in engineered muscle length L (relative to initial length L_0). (*C*) Amplitude of passive tension at 10% strain (L/L_0=1.1). (*D*) Ratio of active tetanus force to passive tension amplitudes at 10% strain. Mean ± SEM; *n* = 4-10 bundles per group.

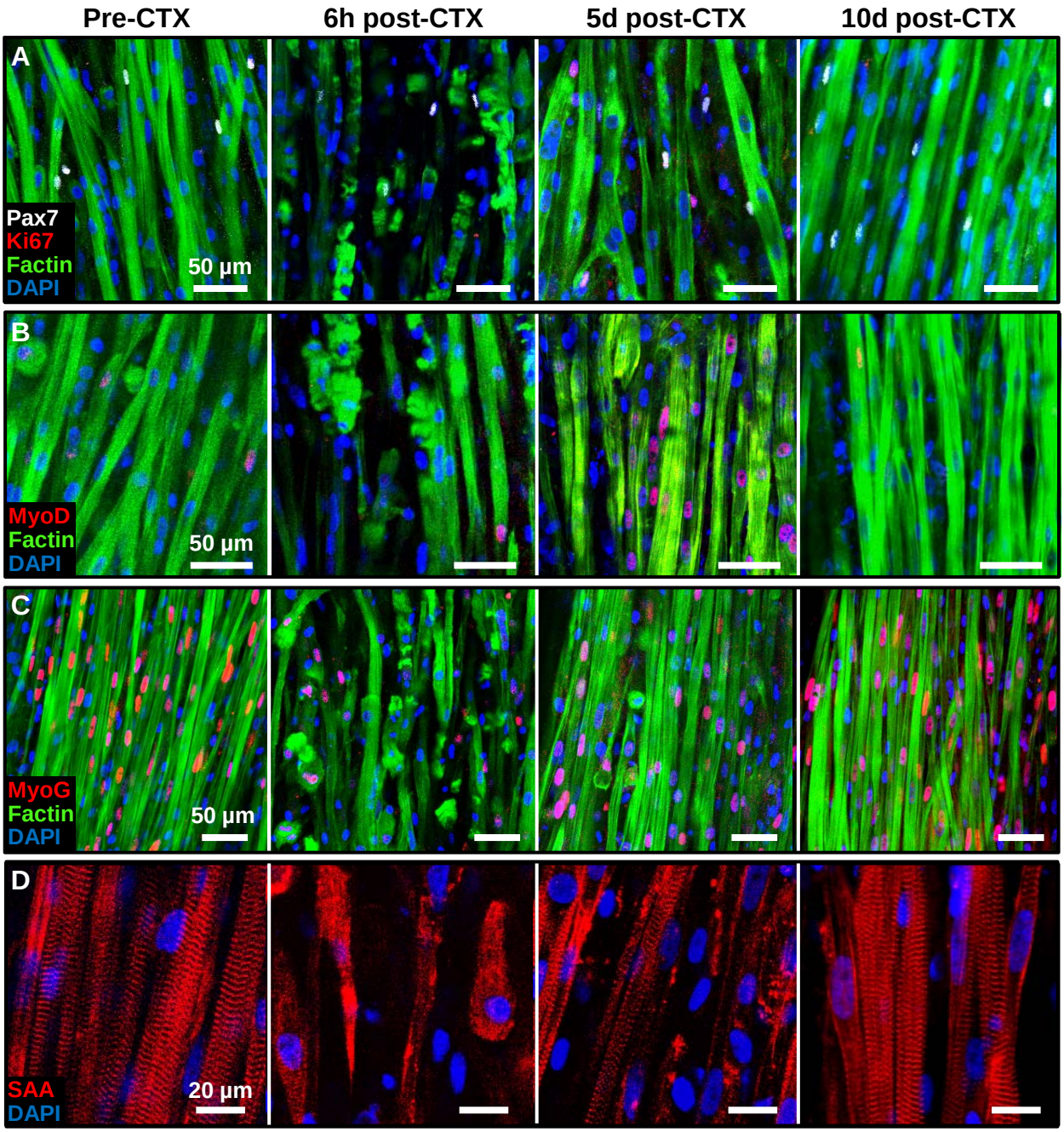

Fig. S6. Regeneration of engineered muscle bundles following cardiotoxin injury in vitro. (*A-C*) Representative images of proliferating satellite cells ($Pax7^{+}/Ki67^{+}$) (*A*), MyoD (*B*), and myogenin (MyoG) (*C*) in 2-wk old engineered muscle bundles prior to cardiotoxin (CTX) administration and 6 hours, 5 days, and 10 days after CTX injury. (*D*) Representative images of the immediate sarcomere destruction following CTX injury and the gradual recovery of sarcomeric structures over the following 10 days of culture.

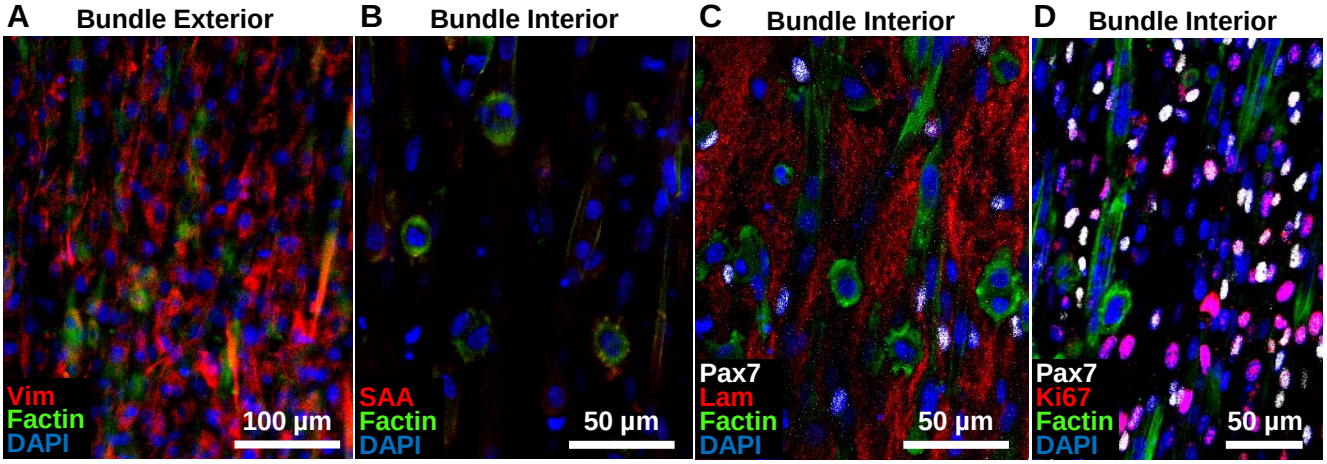

Fig. S7. Structural characterization of 2-day old undifferentiated engineered (UnD) muscle bundles. (*A*) Vimentin (Vim)$^{+}$ fibroblasts were predominantly found at the exterior of the bundle. (*B-C*) Non-fused or newly fusing myogenic cells as well as short immature myotubes were found within the interior of bundle (*B*), along with Pax7^{+} cells and a laminin (Lam)-rich matrix (*C*). *(D)* Undifferentiated myogenic cells inside the bundle were highly proliferative, as evident by the abundant expression of Ki67.

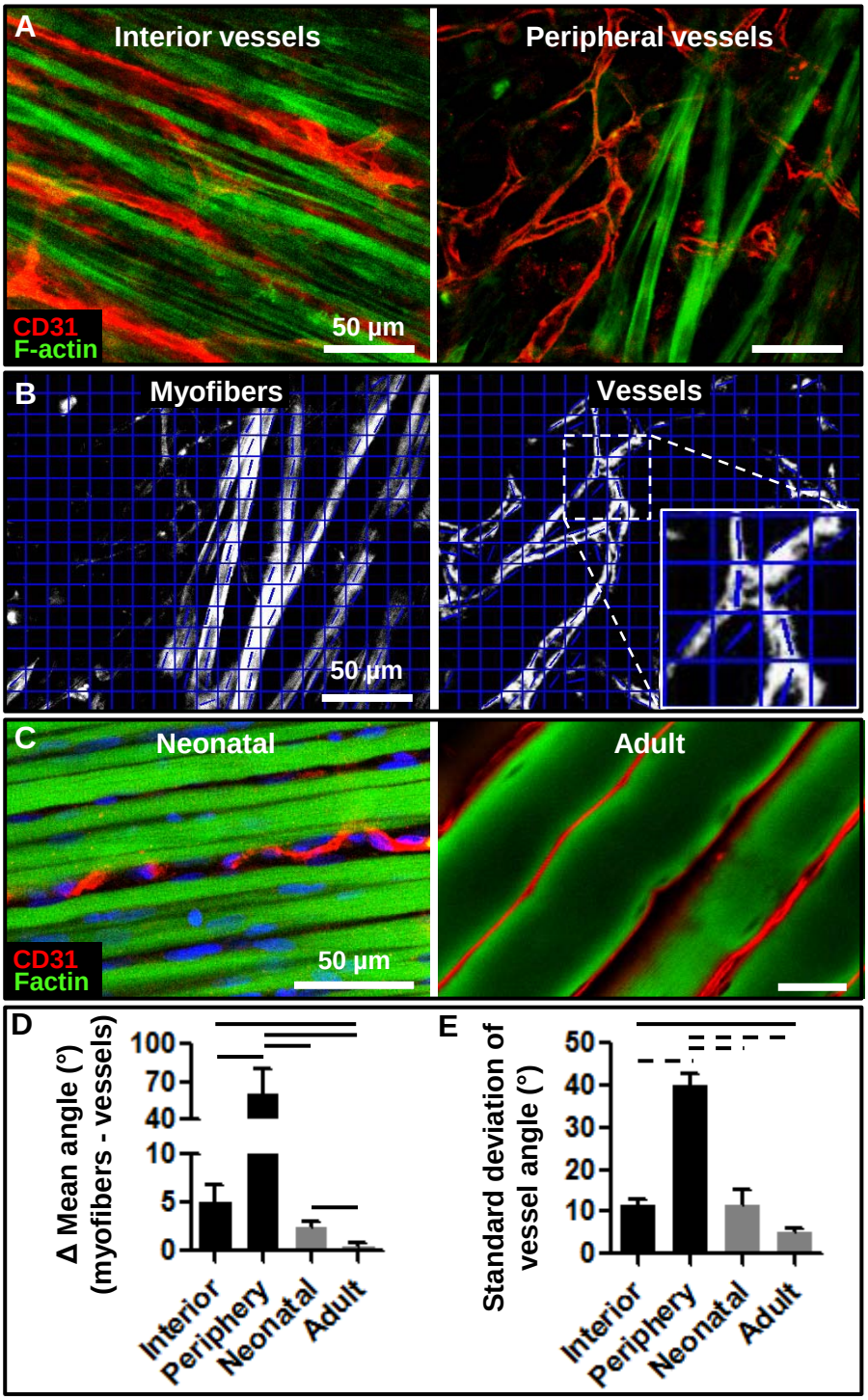

Fig. S8. Vascular organization in implanted engineered muscle bundles. (*A*) Representative images of CD31$^+$ blood vessels and GFP$^+$ myofibers in the interior and periphery of the pre-differentiated (PreD) muscle bundles at 2 wk post-implantation (PI). (*B*) Processed panel A (right) showing separated green and red channels with local myofiber and vessel directions quantified within individual 25x25 pixel (11x11 μm) regions. The close-up inset shows mean direction (angle) of alignment within each pixel denoted by a thin line. (*C*) Representative images of CD31$^+$ vessels in the interior of neonatal and adult muscle. (*D*) Standard deviations of vessel alignment within the interior and periphery of the 2wk PI bundles and native muscles. (*E*) Mean angle differences between average myofiber and vessel directions of alignment. Mean ± SEM; n = 4-8 samples per group (8-10 images per sample); $P<0.05$ and $P<0.001$ between groups denoted by solid and dashed horizontal lines, respectively.

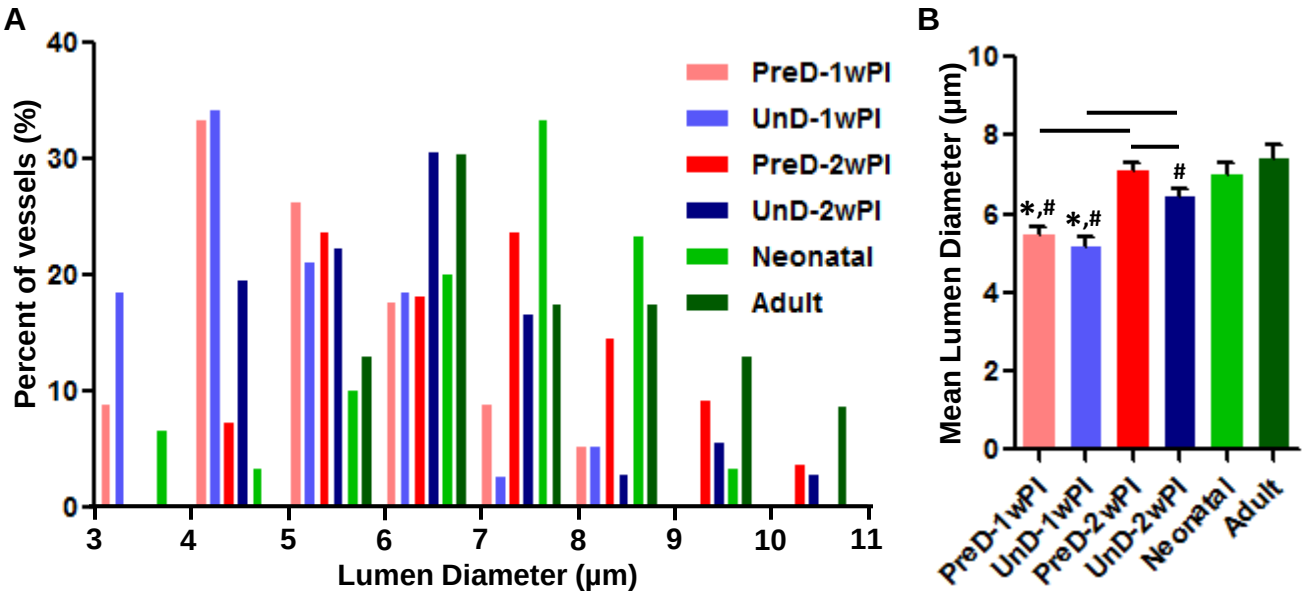

Fig. S9. Capillary lumen diameters in implanted engineered muscle bundles. (*A*) Histogram distribution of lumen diameters within the implanted pre-differentiated (PreD) and undifferentiated (Und) engineered muscle at 1 wk (1wPI) and 2 wk (2wPI) post-implantation (PI) as well in neonatal and adult hind limb muscles. Capillary lumen diameters were measured from cross-sectional images immunostained with F-actin and Von Willebrand Factor (example shown in Figure 3E). (*B*) Mean lumen diameters in 6 studied groups. Mean ± SEM; *n* = 50-70 lumens per group; *P < 0.001 compared to neonatal values, $^{\#}$P < 0.05 compared to adult values, and P < 0.05 between groups denoted by horizontal lines.

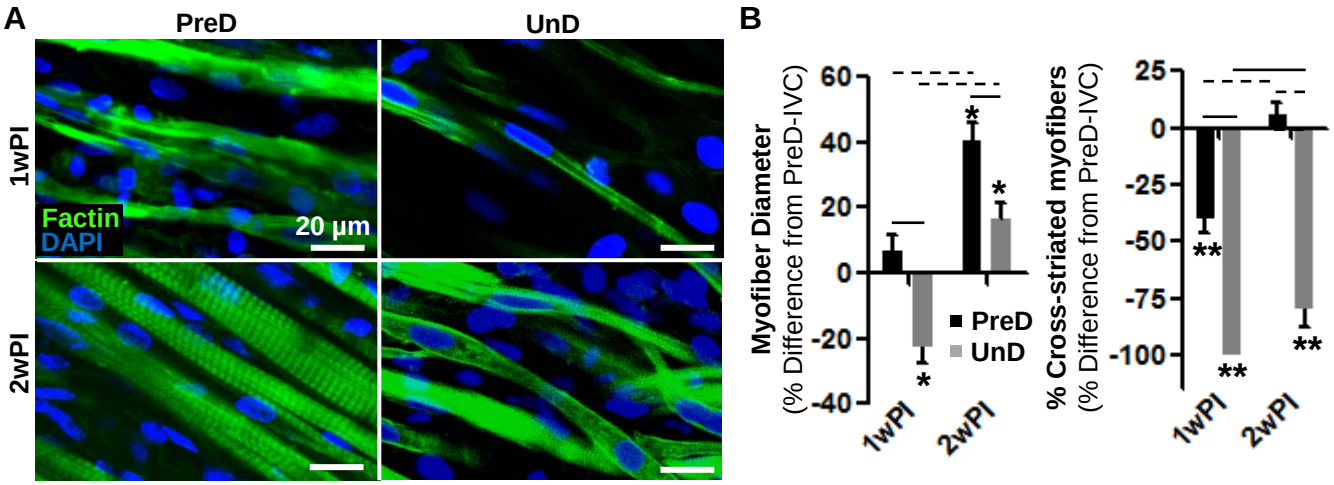

Fig. S10. Myogenesis and structural differentiation of implanted engineered muscle bundles. (*A*) Representative images of myofibers within implanted pre-differentiated (PreD) and undifferentiated (UnD) muscle bundles at 1 wk (1wPI) and 2 wk (2wPI) post-implantation. (*B*) Changes in myofiber diameter and percent of cross-striated myofibers relative to values in PreD bundles cultured for 2 wk *in vitro* (PreD-IVC). Mean ± SEM; *n* = 8-12 bundles (10-20 measurements per bundle) per group; *P<0.05 and **P<0.001 compared to PreD-IVC values; P<0.01 and P<0.001 between groups denoted by solid and dashed horizontal lines, respectively.

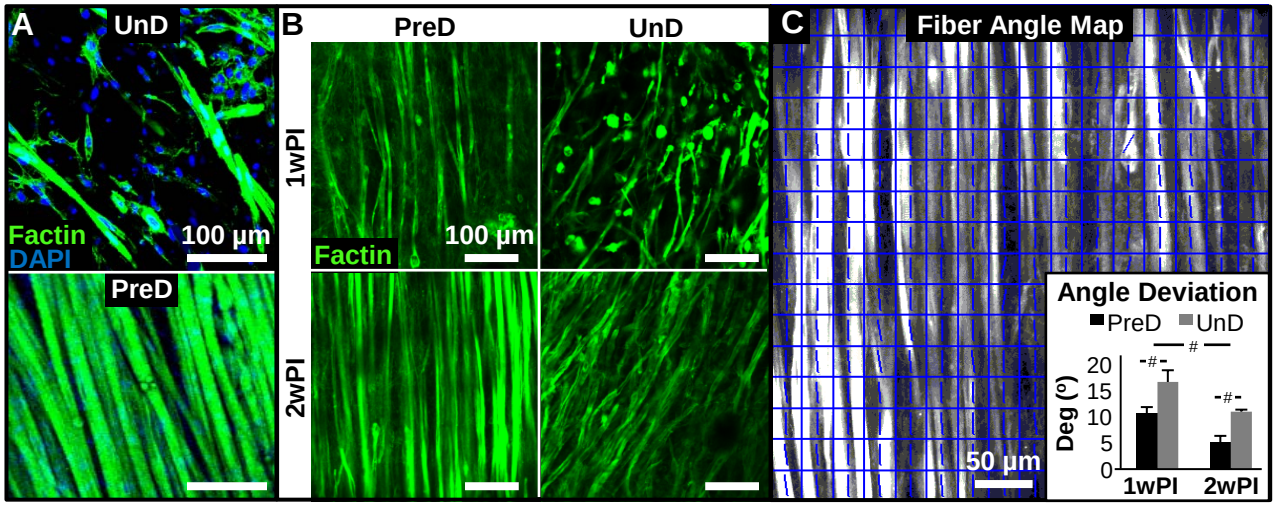

Fig. S11. Myofiber alignment in pre-differentiated and undifferentiated implanted engineered muscle bundles. (*A*) Representative images of myofibers in undifferentiated (UnD) and pre-differentiated (PreD) engineered muscle bundles prior to implantation. (*B*) Representative images of myofiber alignment in PreD and UnD bundles at 1 (1wPI) and 2 wk (2wPI) post-implantation. (*C*) Example map of local myofiber directions within 25x25 pixel (11x11 µm) regions in a PreD bundle. Inset, average local angle deviation from mean myofiber direction (in units of deg). Note more uniform unidirectional alignment (smaller angle deviation) in PreD vs. UnD group. Mean ± SEM, n = 4 bundles per group, $^{\#}P < 0.01$.

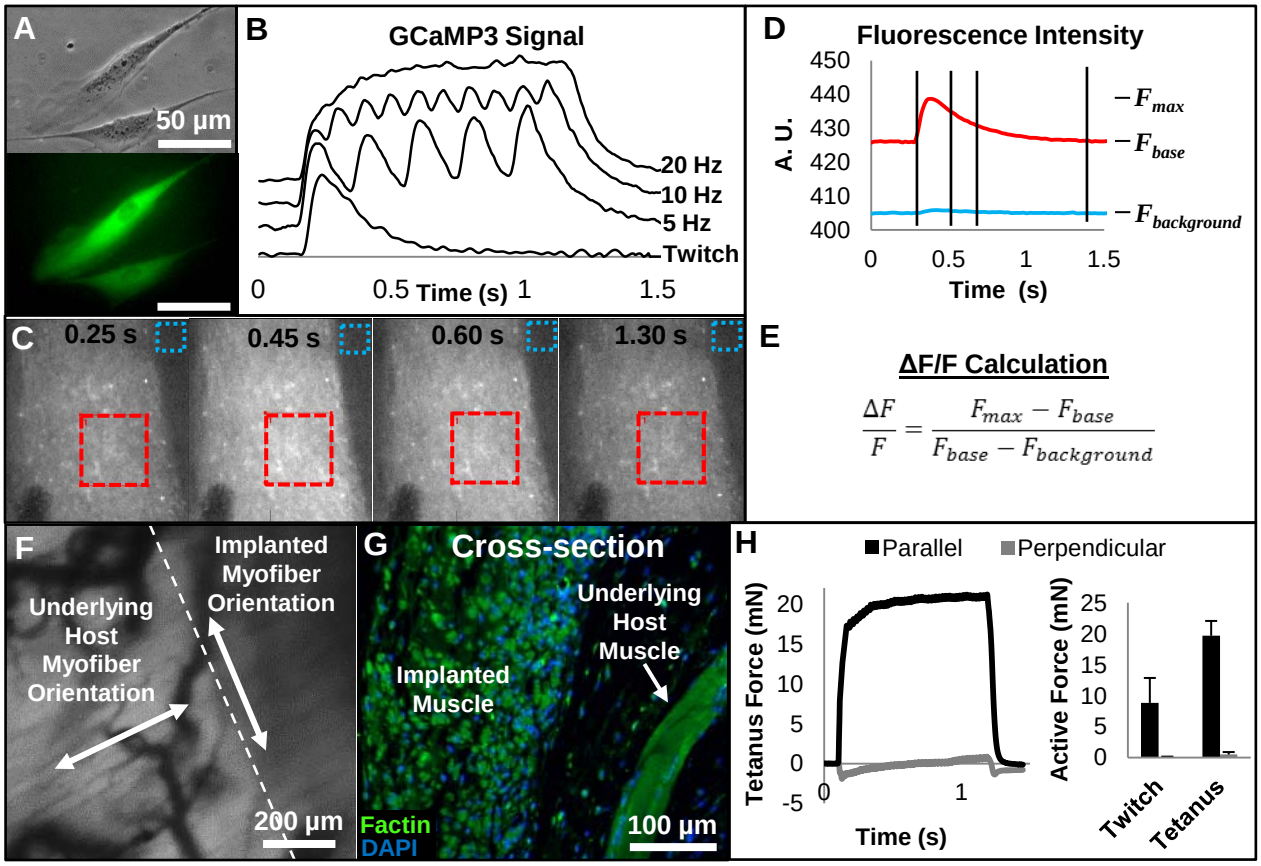

Fig. S12. Measurements of intracellular calcium transient and contractile force generation in implanted engineered muscle bundles. (*A*) Representative brightfield and fluorescent images of myogenic cells transduced with GCaMP3 virus prior to assembly into a muscle bundle. (*B*) Representative GCaMP3 traces from an engineered muscle bundle at various stimulation frequencies. The traces are progressively shifted upwards for improved clarity. (*C*) Select time snapshots of recorded GCaMP3 fluorescence from an explanted muscle bundle during application of an electrical stimulus. (*D*) Averaged fluorescence traces from the red square region within the muscle bundle and blue square region (background) outside of the bundle shown in (*C*). Vertical lines denote times of the snapshots shown in (*C*). (*E*) ΔF/F signal amplitude is calculated using the shown formula. (*F*) Representative brightfield image of an engineered muscle bundle implanted perpendicular to the direction of underlying host muscle fibers within a dorsal window chamber. (*G*) 2 wk post-implantation, transverse cross-section of implanted muscle overlaying longitudinal section of host muscle confirms that two muscles remain perpendicular to each other. (*H*) Representative tetanus force traces and average active forces of control host muscle without implant, measured parallel and perpendicular to host myofiber orientation. Note that in the direction perpendicular to host myofiber orientation (and along the orientation of implanted muscle bundles), the active force generated by the host muscle is negligible. Mean ± SEM; *n* = 3 mice.

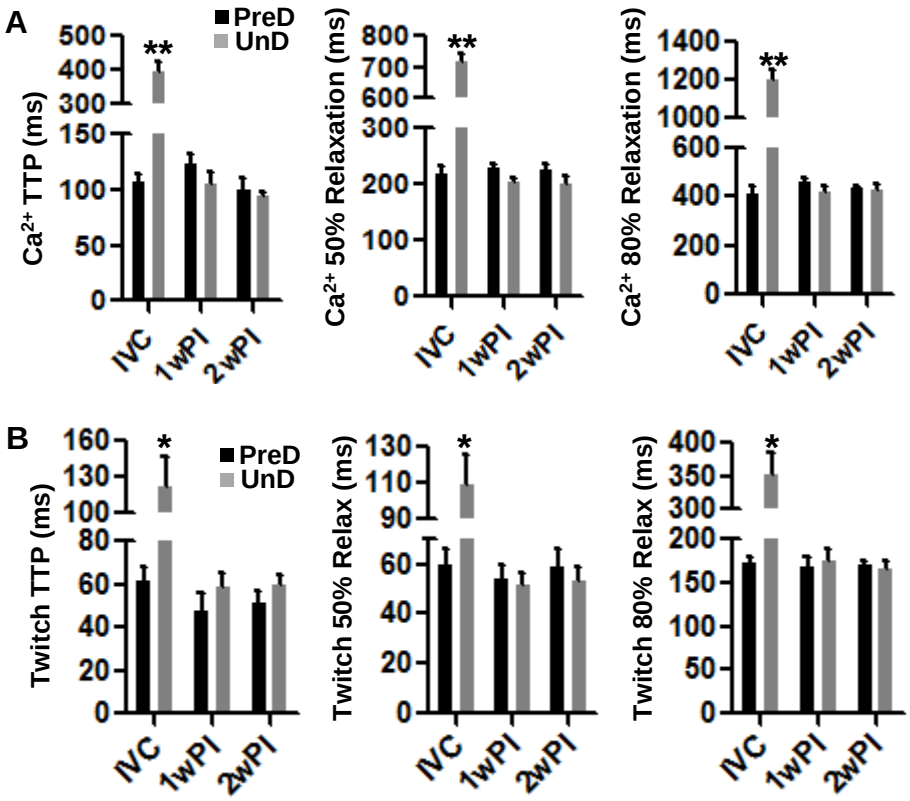

Fig S13. Kinetics of electrically-induced calcium transient and twitch force responses in engineered muscle bundles. Time-to-peak (TTP), 50% relaxation, and 80% relaxation times of (*A*) recorded GCaMP3-calcium transients and (*B*) measured twitch forces during 1 Hz electrical stimulation in pre-differentiated (PreD) and undifferentiated (UnD) *in vitro* (IVC) patches and patches explanted at 1 wk (1wPI) and 2 wk (2wPI) post-implantation. Mean ± SEM; *n* = 6-10 bundles per group; other groups; **P<0.0001 and *P<0.05 compared to all other groups.

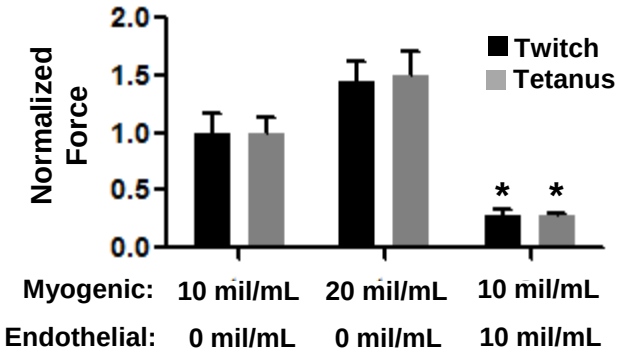

Fig. S14. Effect of co-encapsulation of endothelial and myogenic cells on function of engineered muscle bundles. Twitch and tetanus forces with varying concentrations of myogenic and rat aortic endothelial cells within the engineered muscle bundles normalized to 10 mil/mL myogenic cell group (control). Mean ± SEM; *n* = 4-8 bundles per group; P*<0.01 compared to control.

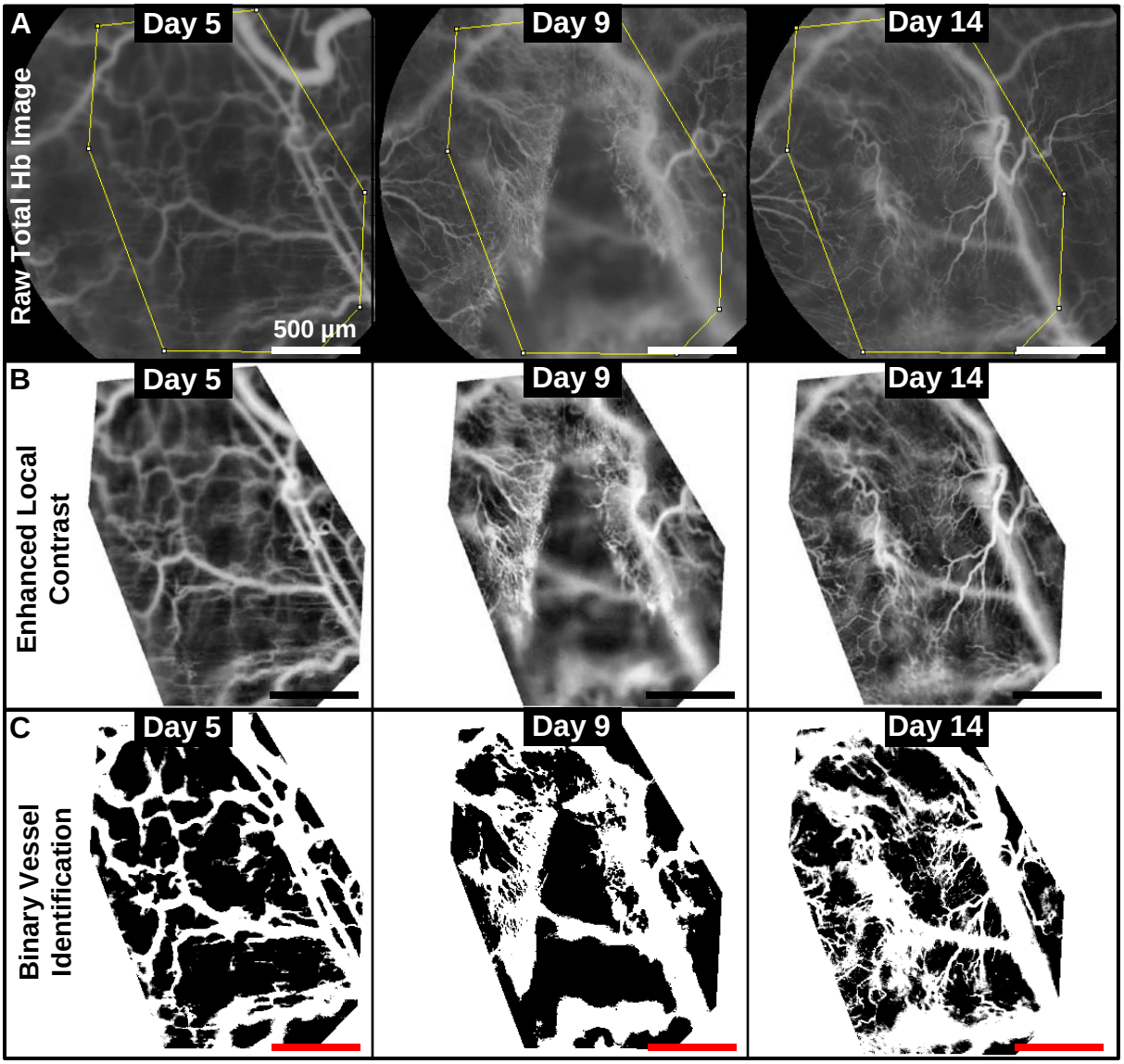

Fig. S15. Method for calculating blood vessel density in implanted engineered muscle bundles. (*A*) Consistent regions of interests (ROIs) were identified within raw intravital images of total hemoglobin concentration for the same implanted bundle at different time points (days) post implantation. Using ImageJ (FIJI) software, local contrast was enhanced (*B*) and blood vessels were identified following conversion of the enhanced into binary images (*C*). From these images, the blood vessel density (i.e., total vessel area per bundle area) was measured in blind fashion.

4) SI Movie Legends

Movie S1. **Engineered muscle contractions.** Representative twitch and tetanus contractions of an unloaded, 2-week old engineered muscle bundle electrically stimulated by a single pulse (10 ms duration, 3 V/mm) or a 40 Hz pulse train, respectively. During culture, ends of the engineered muscle were attached to rectangular Velcro® felts.

Movie S2. Ingrown neovasculature within implanted engineered muscle. Representative intravital recordings of ingrown neovasculature within the implanted engineered muscle (yellow pseudo-color region) at 7 and 14 days post-implantation. Red blood cell flow through the ingrown vessels and spontaneous contractions of engineered muscle are readily observed.

Movie S3. Spontaneous tetanic contraction of implanted engineered muscle. Representative intravital recording of spontaneous tetanic contractions in the implanted engineered muscle (yellow pseudo-color regions) at 14 days post-implantation. Note that during tetanic contraction, blood flow in the ingrown capillaries appears to be transiently haltered.

Movie S4. In vivo recordings of $Ca2^{+}$ transients. Representative intravital recordings of GCaMP3-reported spontaneous Ca^{2+} transients in the implanted pre-differentiated (PreD) and undifferentiated (UnD) engineered muscle bundles (yellow pseudo-color regions) at 14 days post-implantation. Note asynchronous firing of spontaneous Ca^{2+} transients (GCaMP3 flashes) in different myofibers within the implants. Stronger flashes are followed by more forceful contractions.

Movie S5. Ex vivo recordings of $Ca2^{+}$ transients. Representative recordings of GCaMP3-reported, electrically-induced Ca^{2+} transients in the PreD and UnD engineered muscles explanted 14 days post-implantation. Single electrical pulse (10 ms duration, 3 V/mm) induces synchronized, spatially uniform firing of Ca^{2+} transient (GCaMP3 flash) rapidly followed by strong twitch contraction.